HIGH PRESSURE PROPERTIES OF METALS FROM FIRST PRINCIPLE CALCULATIONS: GOLD AS AN EXAMPLE

A THESIS

SUBMITTED TO THE DEPARTMENT OF PHYSICS

AND THE INSTITUTE OF ENGINEERING AND SCIENCE

OF BILKENT UNIVERSITY

IN PARTIAL FULFILLMENT OF THE REQUIREMENTS

FOR THE DEGREE OF

MASTER OF SCIENCE

By

Rasim Volga Ovalı

September, 2004

I certify that I have read this thesis and that in my opinion it is fully adequate, in scope and in quality, as a thesis for the degree of Master of Science.

Assist. Prof. Dr. Oğuz Gülseren (Supervisor)

I certify that I have read this thesis and that in my opinion it is fully adequate, in scope and in quality, as a thesis for the degree of Master of Science.

Assist. Prof. Dr. Ceyhun Bulutay

I certify that I have read this thesis and that in my opinion it is fully adequate, in scope and in quality, as a thesis for the degree of Master of Science.

Assoc. Prof. Dr. Engin Özdaş

Approved for the Institute of Engineering and Science:

Prof. Dr. Mehmet B. Baray
Director of the Institute Engineering and Science

ABSTRACT

HIGH PRESSURE PROPERTIES OF METALS FROM FIRST PRINCIPLE CALCULATIONS: GOLD AS AN EXAMPLE

Rasim Volga Ovalı
M.S. in Physics
Supervisor: Assist. Prof. Dr. Oğuz Gülseren
September, 2004

Metal Au is used extensively in experimental setups as a calibration standard due to its chemical inertness and high structural stability. It is well-known that it has stable fcc structure up to 100 GPa pressure. Furthermore, availability in pure form and, low strength and rigidity makes Au an important material for high pressure material science and geophysics.

In this thesis, our purpose is to calculate the high pressure properties of crystal Au from first principles calculations. A guidance is presented for performing *ab-initio* calculations in the framework of Density Functional Theory (DFT) and using both Local Density Approximation (LDA) and Generalized Gradient Approximation (GGA). The static equation of state (EOS) of Au is obtained up to 500 GPa pressure. The zero-pressure properties of gold (i.e equilibrium volume and total binding energy, bulk modulus, pressure derivative of bulk modulus) is calculated via EOS using Vinet formalism. The structural phase transformation (fcc to bcc phase) is observed at ultrahigh pressure regime. The band structures and density of states belonging to these phases are discussed at zero and 600 GPa pressures. The elastic properties (for example; elastic constants, aggregate constants, sound velocities, aggregate velocities) of Au is calculated and compared with experimental data and similar theoretical studies. Finally, calculated phonon spectrum for various hydrostatic pressure values is compared with experimental data.

Keywords: Equation of state, elastic constants, vibrational spectrum, phonons, gold, high pressure, first-principle calculations.

ÖZET

TEMEL PRENSİPLER HESABI İLE METALLERİN YÜKSEK BASINÇ ÖZELLİKLERİ: ÖRNEK OLARAK ALTIN METALİ

Rasim Volga Ovalı
Fizik, Yüksek Lisans
Tez Yöneticisi: Yard. Doç. Dr. Oğuz Gülseren
Eylül, 2004

Altın, yüksek kimyasal ve yapısal kararlılık göstermesi nedeniyle deneysel düzeneklerde kalibrasyon standardı olarak sıkça kullanılmaktadır. Ayrıca altının 100 GPa basıncına kadar kararlı fcc yapısına sahip olduğu iyi bilinmektedir. Bunun yanı sıra kolaylıkla saf halde elde edilebilmesi ve kolay sıkıştırılabilir olması malzeme bilimi ve yer bilimi açısından altını önemli bir madde haline getirmektedir.

Bu tezde amaç, altın metalinin değişik kristal yapılarını temel prensiplere dayalı kuantum mekaniksel hesaplamalar ile iki farklı yoğunluk fonksiyonu (LDA ve GGA) için incelemektir. Tezin ilk bölümü, hesaplamalarda temel olarak kullandığımız Yoğunluk Fonksiyoneli Teorisi ve temel prensipler hesabı konularını açıklamaktadır. Daha sonraki bölümde, sıfır sıcaklıkta altının fcc yapısı için 500 GPa basıncına kadar basınç-hacim eğrisi çıkartıldı. Hesaplanan basınç-hacim eğrisi değişik durum denklemleri ile karşılaştırılarak bulk modülü, bulk modülün türevi ve denge hacmi hesaplandı. Bcc ve hcp yapılarıda toplam bağlanma enerjileri hesaplanarak yüksek basınçta faz değişimi olabileceği görüldü. 0 ve 600 GPa basınç değerlerinde fcc ve bcc fazlarının band yapıları ve durum yoğunlukları hesaplanarak karşılaştırıldı. Bunun yanı sıra elastik sabitler ve fonon spektrumu, değişik hidrostatik basınç değerleri için hesaplanarak deneysel verilerle karşılaştırıldı.

Anahtar sözcükler: Durum denklemi, elastik sabitler, titreşim spektrumu, fononlar, altın, yüksek basınç, temel prensipler hesabı.

Acknowledgement

I am indebted to Assist. Prof. Dr. Oğuz Gülseren for constant help, support and encouragement as a supervisor during my MS.

I would like to thank my group member Deniz Çakır for improving my knowledge and his great effort to explain things.

I am grateful to my colleagues Engin Durgun, Sefa Dağ, Haldun Sevinçli, Sevilay Sevinçli, Levent Subaşı and Sefaattin Tongay for their friendship and endless help during my thesis work.

Personally, I would like to thank Koray Aydın, Sinem Binicioğlu Çetiner, Selin Damla Erdoğan, Güneş Erdoğan, Orçun Ergün, Serdar Özdemir, Barış Öztop, Kerim Savran, Cem Sevik, Emre Taşgın and Muhammed Yönaç for their friendship during my undergraduate and graduate study.

At last, I wish to thank my mother, Pakize Ovalı and my sister Burçak whom I love the most. I dedicate this thesis to my father, Yaşar Ovalı.

Contents

1 INTRODUCTION **1**

2 THEORETICAL BACKGROUND **3**

2.1 Introduction 3

2.2 Born-Oppenheimer Approximation 4

2.3 Hartree and Hartree-Fock Methods 5

2.4 Density Functional Theory 7

2.4.1 Thomas-Fermi Theory 9

2.4.2 Hohenberg-Kohn Theorem 10

2.4.3 Kohn-Sham Energy Functional 11

2.4.4 Kohn-Sham Equations 12

2.5 Local Density Approximation 13

2.6 Generalized Gradient Approximation 14

2.7 Computational Details 15

2.7.1 Bloch's Theorem 15

2.7.2 Plane-wave basis sets 16

2.7.3 Pseudopotential Approximation 17

2.7.4 k-point sampling 18

3 LITERATURE SURVEY **20**

3.1 Introduction 20

3.2 Experimental Results for Gold 20

3.3 Computational Results for Gold 22

4 EQUATION OF STATE OF GOLD **29**

4.1 Introduction 29

4.2 Computational Details 30

4.3 Results for Gold Crystal 30

4.4 Structural Phase Transition of Gold 36

5 ELASTIC PROPERTIES OF GOLD **39**

6 PHONON DISPERSION RELATIONS **52**

7 CONCLUSION **58**

List of Figures

2.1 A schematic diagram of core potential, pseudopotential and corresponding wave functions. Above r_c these two potentials are same. 18

3.1 Heinz *et al.* [22] diamond-anvil cell data and Birch-Murnaghan [23][24][25] equation of state fit for Au. 21

3.2 The equation of state of Au at 0 K obtained by Godwal *et al.* [31] using LMTO calculations. The heavy solid line is the calculated data, and other lines are the three equations of state: Vinet *et al.* [32][33][34], Dodson [35], and Birch [23]. Upper panel shows the pressure difference between these equations of state and LMTO calculations. 23

3.3 The figures show electron populations and partial pressured (in units rydbergs) for s, p, d, and f bands of gold as a function of relative volume, respectively. The calculations were based on LMTO method. 23

3.4 Two types of elastic anisotropy factor, the Zener ratio A_Z and acoustic anisotropy factor A_a. The figure is taken form Tsuchiya *et al.* [40] 25

3.5 The figures shows the calculated density of states for fcc and hcp phases at two different volumes, $V/V_0 = 1.0$ and $V/V_0 = 0.5$. The figures are taken from Ahuja *et al.* [44] 27

3.6 Söderlind [45] calculations is shown in order to demonstrate fcc-hcp-bcc structural phase transitions of Au. 28

4.1 The test to determine the energy cutoff for plane waves. 31

4.2 An example of k-point test. 31

4.3 The variation of cohesive energy per atom with lattice constant a_0. Both LDA and GGA results are shown. 32

4.4 Equation of state of Au. Open symbols are the current results. Filled symbols are the experimental data of Heinz and Jeanloz [22] and Duffy *et al.* [30]. The output data are also shown for LDA and GGA. The small figure zooms to the 0-125 GPa pressure range. 35

4.5 Pressure as a function of relative volume. Vinet EOS fits of LDA and GGA results are represented with open symbols. Two experimental data (Heinz-Jeanloz and Duffy) are also shown. The small figure shows the similar data at 0-100 Gpa pressure range. 35

4.6 Variation of energy residues of Vinet and Birch-Murnaghan types of equation of states with respect to lattice volume. 36

4.7 Energy difference between the bcc, hcp and the fcc structures. The fcc structure is used as the zero-energy reference level. The x-axis is the relative volume. 37

4.8 Energy differences between the bcc, hcp and the fcc structures for gold as a function of pressure. The fcc phase is used as the zero-energy reference level. 38

5.1 Static elastic constants of Au as a function of pressure. Filled squares are the calculated values, filled circles are the x-ray diffraction data of Duffy *et al.* [30], and filled triangles are the DFT calculations of Greeff [46] and Tsuchiya [40]. The figure inside shows the same physical quantities at 10-40 GPa pressure range. 42

5.2 Variation of tetragonal shear modulus, c_S, with pressure. Filled squares are the current results. Filled circles are the experimental data of Duffy *et al.* [30], filled triangles are the computational data of Greeff [46] and Tsuchiya [40]. 44

5.3 Pressure dependence of bulk modulus. The small figure shows the same quantities at 200-450 GPa pressure range. An experimental data (Duffy *et al.* [30] and two computational data (Greeff [46], Tsuchiya [40])are also shown in figure. 44

5.4 Pressure dependence of elastic anisotropy, A_Z. 45

5.5 Sound velocities of Au as a function of pressure. Solid lines are two transverse and one longitudinal sound velocities along [110] direction. Brackets indicates the polarization directions. Dotted lines are the isotropic aggregate velocities, ν_P, ν_S, and ν_B. 46

5.6 Scalar relativistic LDA electronic band structure and density of states for fcc Au at zero pressure. The energies are given relative to the Fermi level, the dotted line. 47

5.7 Scalar relativistic LDA electronic band structure and density of states for fcc Au at 200 GPa pressure. The energies are given relative to the Fermi level, the dotted line. 48

5.8 Scalar relativistic LDA electronic band structure and density of states for fcc Au at 600 GPa pressure. The energies are given relative to the Fermi level, the dotted line. 49

5.9 Scalar relativistic LDA electronic band structure and density of states for bcc Au at zero pressure. The energies are given relative to the Fermi level, the dotted line. 50

5.10 Scalar relativistic LDA electronic band structure and density of states for bcc Au at 600 GPa pressure. The energies are given relative to the Fermi level, the dotted line. 51

6.1 Phonon dispersion relation for fcc Au at zero pressure. The filled circles are the experimental data of Lynn *et al.* [29]. The high symmetry points and transverse and longitudinal branches are marked in the figure. 54

6.2 Phonon dispersion relation for fcc Au at 67 GPa pressure. 55

6.3 The variation of zone boundary phonons as a function of pressure. 56

6.4 The phonon density of states at 0, 67, 147 and 283 GPa pressures. 57

List of Tables

3.1 Golding *et al.* [26], Hiki *et al.* [27] and Daniels *et al.* [28] results of zero-pressure elastic constants and pressure derivatives of Au. The elastic constants are in units of GPa. 22

3.2 Khein *et al.* [37] results of lattice constant and bulk modulus at equilibrium position using both LDA and GGA. The numbers inside the parenthesis shows the percentage error relative to experiment. 24

3.3 Tsuchiya *et al.* [40] findings of elastic constants and pressure derivatives for Au at zero-pressure using LDA. The elastic constant are in units of GPa. . . 24

3.4 Boettger's [42] results of equilibrium volume, bulk modulus and pressure derivative of bulk modulus. The LCGTO-FF method has been used. The table also shows the results with spin-orbit-coupling effects. 26

4.1 Equilibrium primitive cell volume, cohesive energy, bulk modulus and its pressure derivative are given for LDA and GGA approximations and two experimental data. The numbers in the parenthesis are the errors relative to Heinz-Jeanloz experimental data. Note that the values of last line calculated by analyzing the experimental data with BM EOS. 34

5.1 Elastic constants and pressure derivatives of three stiffness constants of Au at zero-pressure. LDA and GGA results and various experimental and computational data are given. The references with asterisk are the experimental studies. The units of elastic constants are GPa. The last line shows the LDA results at experimental equilibrium lattice constant. 41

5.2 Zero-pressure Voigt [49] (assumes uniform strain) and Reuss [50] (assumes uniform stress) assumptions of averaged shear modulus. $G_{VRH}=(G_V+G_R)/2$. All shear modulus have the units of GPa. The references with asterisk are the experimental works. The last line shows the LDA calculation at experimental equilibrium lattice constant. 43

Chapter 1

INTRODUCTION

With the development of diamond-anvil cell (DAC) and shock-wave measurement techniques, the attainable pressure range is increased dramatically. Using DAC techniques, pressures of 200-300 GPa can be reached in a laboratory. More extreme pressures are also on the horizon. The most widely used calibration standard in these experiments is metal gold because of its chemical inertness, structural stability, availability in pure form and low strength and rigidity. Thus the chemical and physical properties of Au has to be known even at extreme pressures.

The total energy calculations is a powerful method to obtain the physical properties because nearly all physical properties are related with total energy or the differences between total energies [1]. Studies on total-energy techniques show that method can be used to predict equilibrium lattice constants, bulk moduli, phonons, piezoelectric constants, and phase transition pressures and temperatures accurately. Thus, many computational techniques were developed in order to calculate the physical properties of materials. The name *ab-initio* usually refers to the methods which require only the specification of the ions present [1]. The most successful of these methods is the total-energy pseudopotential method.

Due to the reasons described in the above paragraphs, purpose of this thesis is to obtain physical properties of Au at ambient and ultra high pressures using

first principles calculations. The equation of state of Au is calculated up to 500 GPa with two approximation methods, Local Density Approximation (LDA) and Generalized Gradient Approximation (GGA). The comparison of LDA and GGA functionals is also presented. Moreover, the data is analyzed in terms of different EOS forms. The calculations were repeated for different phases for Au (such that bcc and hcp) and a phase transition was observed at ultrahigh pressure regime. Furthermore, the total energy calculations were used to calculate the elastic properties. Three elastic stiffness constants (c_{11}, c_{12} and c_{44}), tetragonal shear modulus, bulk modulus and their pressure dependencies are presented. The aggregate properties are also included. Band structure and density of states was calculated for fcc structure at 0 GPa, 200 GPa and 600 GPa and for bcc structure at 0 GPa and 600 GPa. At the end phonon dispersion relations and pressure dependencies of zone boundary phonons were calculated.

The thesis is organized as follow. In chapter 2, the theoretical background and computation method are presented. At the end of the chapter some computational details are also discussed. In Chapter 3, both computational and experimental studies in the literature are summarized. Chapters 4, 5 and 6 are the result chapters. The equation of state, related properties and phase transition at ultrahigh pressures are given in Chapter 4. Chapter 5 is related with elastic properties of Au. In Chapter 6 phonon dispersion relations are presented. Finally, Chapter 7 concludes the thesis.

Chapter 2

THEORETICAL BACKGROUND

2.1 Introduction

The physical and chemical properties of matter can be exactly determined by solving many-body Schrödinger equation. But in many cases this task is difficult because too many particles interacting with each other (i.e electrons and ions, and consider Avogadro number $\sim 10^{23}$) and Schrödinger equation cannot be easily decoupled into a set of independent equations. Additionally a system consists of different kinds of particles which obey different particular statistics. In the general form, the Hamiltonian of such a system is:

$$\begin{aligned} H &= -\sum_{I=1}^{P}\frac{\hbar^2}{2M_I}\nabla_I^2 - \sum_{i=1}^{N}\frac{\hbar^2}{2m}\nabla_i^2 + \frac{e^2}{2}\sum_{I=1}^{P}\sum_{J\neq I}^{P}\frac{Z_I Z_J}{|\mathbf{R}_I - \mathbf{R}_J|} \\ &+ \frac{e^2}{2}\sum_{i=1}^{N}\sum_{j\neq i}^{N}\frac{1}{|r_i - r_j|} - e^2\sum_{I=1}^{P}\sum_{i=1}^{N}\frac{Z_I}{|\mathbf{R}_I - r_j|} \\ &= T_N + T_e + V_{NN}(\mathbf{R}) + V_{ee}(\mathbf{r}) + V_{Ne}(\mathbf{r},\mathbf{R}) \end{aligned} \tag{2.1}$$

where $\mathbf{R} = \{\mathbf{R}_I\}$, $I = 1...P$, is a set of P nuclear coordinates, and $\mathbf{r} = \{\mathbf{r}_i\}$, $i = 1...N$, is a set of N electronic coordinates. Then the following Schrödinger equation is:

$$H\Psi_i(\mathbf{r},\mathbf{R},t) = E_i\Psi_i(\mathbf{r},\mathbf{R},t)$$
$$\left[T_N + T_e + V_{ee}(\mathbf{r}) + V_{NN}(\mathbf{R}) + V_{Ne}(\mathbf{r},\mathbf{R})\right]\Psi_i(\mathbf{r},\mathbf{R},t) = E_i\Psi_i(\mathbf{r},\mathbf{R},t) \quad (2.2)$$

The electrons obey the Fermi-Dirac statistics so the electronic wave functions should be antisymmetric and the nuclei can be fermions, bosons or distinguishable particles.

To solve the Schrödinger equation some approximations are necessary. The first one is Adiabatic Approximation (Born-Oppenheimer approximation).

2.2 Born-Oppenheimer Approximation

Since the time scales of nuclear and electronic motions are different, such that the velocity of the nucleus is much slower than the electrons due to large mass difference between electrons and nuclei, the nuclei can be treated as in the same stationary state of the electronic Hamiltonian. Then the full wave function can be separable into nuclear and electronic wave functions. The nuclear wave function may vary in time because of the coulombic interactions but the electronic wave function instantaneously adjust itself to the nuclear wave function because of the very fast response of electrons to the ionic motion. Then the full wave function factorizes as:

$$\Psi_i(\mathbf{r},\mathbf{R},t) = \Theta_m(\mathbf{R},t)\Phi_m(\mathbf{R},\mathbf{r}) \quad (2.3)$$

where $\Theta_m(\mathbf{R},t)$ and $\Phi_m(\mathbf{R},\mathbf{r})$ are nuclear and electronic wave functions respectively. Then the decoupled adiabatic Schrödinger equations of electrons and nuclei are:

$$\begin{aligned}\left[T_e + V_{ee}(\mathbf{r}) + V_{Ne}(\mathbf{r},\mathbf{R})\right]\Phi_m(\mathbf{R},\mathbf{r}) &= \varepsilon_m(\mathbf{R})\Phi_m(\mathbf{R},\mathbf{r}) \\ \left[T_N + V_{NN}(\mathbf{R}) + \varepsilon(\mathbf{R})\right]\Theta_m(\mathbf{R},t) &= i\hbar\frac{\partial}{\partial t}\Theta_m(\mathbf{R},t) \quad (2.4)\end{aligned}$$

where m is any electronic eigenstate but in the literature it is taken as ground state in many applications. If we neglect the quantum effects in ionic dynamics, the time-dependent ionic Schrödinger equation can be replaced by classical Newtonian equation of motion as:

$$\begin{aligned} \frac{\partial^2 \mathbf{P}_I(t)}{\partial t^2} &= -\nabla_I E_0(\mathbf{R}) \\ E_0(\mathbf{R}) &= \varepsilon_0(\mathbf{R}) + V_{NN}(\mathbf{R}) \end{aligned} \tag{2.5}$$

Then the force ($\nabla_I E_0(\mathbf{R})$) acting on nucleus contains contributions from ion-ion interaction and a term from the gradient of the electronic total energy which is given as the expectation value of gradient of the electronic Hamiltonian in the ground state from Hellmann-Feynman theorem.

$$\begin{aligned} \nabla_I \varepsilon(\mathbf{R}) &= \frac{\partial}{\partial \mathbf{R}_I} \langle \Phi_0 | H_e(\mathbf{R}) | \Phi_0 \rangle \\ &= \langle \nabla_I \Phi_0 | H_e(\mathbf{R}) | \Phi_0 \rangle \\ &+ \langle \Phi_0 | \nabla_I H_e(\mathbf{R}) | \Phi_0 \rangle \\ &+ \langle \Phi_0 | H_e(\mathbf{R}) | \nabla_I \Phi_0 \rangle \\ &= \langle \Phi_0 | \nabla_I H_e(\mathbf{R}) | \Phi_0 \rangle \end{aligned} \tag{2.6}$$

First and third terms are vanish due to variational property of the ground state.

Now we are left with solving the electronic Schrödinger equation. But again this is not an easy job even numerically and some approximations should be necessary.

2.3 Hartree and Hartree-Fock Methods

In 1928 Hartree [2] proposed a method for solving many-body electronic Schrödinger equation. According to that the many-electron wave function can

be written as a product of one-electron wave functions and each electron sees an effective potential generating by other electrons and ions. Then the ground state of the many body Hamiltonian can be solved from variational principle. The Hartree formulation can be summarized as:

$$\Phi(\mathbf{R}.\mathbf{r}) = \prod_i \varphi(\mathbf{r}_i) \tag{2.7}$$

$$\left(-\frac{\hbar^2}{2m}\nabla^2 + V_{eff}^{(i)}(\mathbf{R},\mathbf{r})\right)\varphi_i(\mathbf{r}) = \varepsilon_i\varphi_,(\mathbf{r}) \tag{2.8}$$

The effective potential is the sum of the potential of ions at positions $\mathbf{R}$ ($V(\mathbf{R},\mathbf{r})$) and the electrostatic potential generated by the charge distribution $\sum_{j\neq i}^{N}\rho_j(\mathbf{r})$ as:

$$V_{eff}^{(i)}(\mathbf{R},\mathbf{r}) = V(\mathbf{R},\mathbf{r}) + \int \frac{\sum_{j\neq i}^{N}\rho_j(\mathbf{r}')}{|\mathbf{r}-\mathbf{r}'|}d\mathbf{r}' \tag{2.9}$$

where

$$\rho_j(\mathbf{r}) = |\varphi_j(\mathbf{r})|^2 \tag{2.10}$$

Since the effective potential depends on the eigenstate, thus the solution, this becomes Self-Consistent Field (SCF) problem which has to be solved iteratively. The method works as follow. Starting from a appropriate trial wave function the electronic density ($\rho_j(\mathbf{r})$) can be found from Eq. 2.10 and effective potential can be calculated from Eq. 2.9 After solving Schrödinger equation, the procedure is repeated several times with new wave functions until the self-consistency is achieved. The total energy of the system is then:

$$E_H = \sum_{n=1}^{N}\varepsilon_n - \frac{1}{2}\int\int\frac{\rho(\mathbf{r})\rho(\mathbf{r}')}{|\mathbf{r}-\mathbf{r}'|}d\mathbf{r}d\mathbf{r}' \tag{2.11}$$

where $\rho(r)$ is the final electronic charge density and ε_n is the eigenvalue corresponding to n^{th} electron. Note that the total electronic energy is not just the sum of eigenvalues of electrons because the effective potential in the formulation is counted twice.

Since the electrons are fermions, Hartree formulation can be improved by considering the Pauli exclusion principle such that the many-electron wave function

is replaced by the antisymmetrized many-electron wave function in the from of Slater [3] determinant as:

$$\Phi(\mathbf{R},\mathbf{r}) = \frac{1}{\sqrt{N!}} \begin{vmatrix} \varphi_1(\mathbf{r}_1,\sigma_1) & \varphi_1(\mathbf{r}_2,\sigma_2) & ... & \varphi_1(\mathbf{r}_N,\sigma_N) \\ \varphi_2(\mathbf{r}_1,\sigma_1) & \varphi_2(\mathbf{r}_2,\sigma_2) & ... & \varphi_1(\mathbf{r}_N,\sigma_N) \\ ... & ... & ... & ... \\ \varphi_N(\mathbf{r}_1,\sigma_1) & \varphi_N(\mathbf{r}_2,\sigma_2) & ... & \varphi_N(\mathbf{r}_N,\sigma_N) \end{vmatrix} \tag{2.12}$$

The approximation is called Hartree-Fock [4] and works similar as Hartree approximation except that the additional coupling term (i.e exchange) appears in the Schrödinger equation as:

$$\left(-\frac{\hbar^2}{2m}\nabla^2 + V(\mathbf{R},\mathbf{r}) + \int \frac{\sum_{\sigma',j=1}^{N} \rho_j(\mathbf{r}',\sigma')}{|\mathbf{r}-\mathbf{r}'|} d\mathbf{r}'\right)\varphi_i(\mathbf{r},\sigma) - \\ -\sum_{j=1}^{N}\left(\sum_{\sigma'}\int \frac{\varphi_j^*(\mathbf{r}',\sigma')\varphi_i(\mathbf{r}',\sigma')}{|\mathbf{r}-\mathbf{r}'} d\mathbf{r}'\right)\varphi_j(\mathbf{r},\sigma) = \sum_{j=1}^{N}\lambda_{ij}\varphi_j(\mathbf{r},\sigma) \tag{2.13}$$

Both methods are simple but have some disadvantages. First, the computational time increases rapidly with increasing number of electrons. Second, many-body correlations are neglected in the formulation.

2.4 Density Functional Theory

In 1927-1928 Thomas and Fermi proposed that the electronic charge density is the fundamental variable of the many-electron problem [5][6] and the Thomas-Fermi theory is the starting point of the *Density Functional Theory* (DFT). Today, the DFT calculations is the common way of total energy calculations in condensed matter physics.

The main problem in total energy calculations of a system composed of N interacting electrons in an external field is to take the correlations effects into

account. These are due to electron-electron interactions. The total energy can be written as before:

$$E = \langle\Phi|\widehat{T} + \widehat{V} + \widehat{V}_{ee}|\Phi\rangle = \langle\Phi|\widehat{T}|\Phi\rangle + \langle\Phi|\widehat{V}|\Phi\rangle + \langle\Phi|\widehat{V}_{ee}|\Phi\rangle \tag{2.14}$$

where T is the kinetic energy, V is the energy due to ions or external field and V_{ee} is the electron-electron interaction. We now concentrate on the electron-electron interaction term which can be written as:

$$V_{ee} = \langle\Phi|\widehat{V}_{ee}|\Phi\rangle = \left\langle \Phi \left| \frac{1}{2}\sum_{i=1}^{N}\sum_{j\neq}^{N} \frac{1}{|\mathbf{r}_i - \mathbf{r}_j|} \right| \Phi \right\rangle = \int \frac{\rho_2(\mathbf{r},\mathbf{r}')}{|\mathbf{r}-\mathbf{r}'|} d\mathbf{r}d\mathbf{r}' \tag{2.15}$$

where $\rho_2(\mathbf{r},\mathbf{r}')$ is the two-body density matrix and can be defined in terms of annihilation and creation operators $(a, a^\dagger)$ for electrons as:

$$\rho_2(\mathbf{r},\mathbf{r}') = \frac{1}{2}\sum_{\sigma,\sigma'}\langle\Phi|a^\dagger_\sigma(\mathbf{r})a^\dagger_{\sigma'}(\mathbf{r}')a_{\sigma'}(\mathbf{r}')a_\sigma(\mathbf{r})|\Phi\rangle \tag{2.16}$$

Now we define the two-body correlation function $g(\mathbf{r},\mathbf{r}')$ as:

$$\rho_2(\mathbf{r},\mathbf{r}') = \frac{1}{2}\rho(\mathbf{r},\mathbf{r})\rho(\mathbf{r}',\mathbf{r}')g(\mathbf{r},\mathbf{r}') \tag{2.17}$$

where $\rho(\mathbf{r},\mathbf{r}')$ is the one-body density matrix. With the definitions:

$$\rho(\mathbf{r},\mathbf{r}') = \sum_\sigma \rho_\sigma(\mathbf{r},\mathbf{r}') \tag{2.18}$$

$$\rho_\sigma(\mathbf{r},\mathbf{r}') = \langle\Phi|a^\dagger_\sigma(\mathbf{r})a_\sigma(\mathbf{r}')|\Phi\rangle \tag{2.19}$$

the electron-electron interaction energy of Eq. 2.15 from equations 2.16, 2.17, 2.18 and 2.19 will be:

$$V_{ee} = \frac{1}{2}\int \frac{\rho(\mathbf{r})\rho(\mathbf{r}')}{|\mathbf{r}-\mathbf{r}'|} d\mathbf{r}d\mathbf{r}' + \frac{1}{2}\int \frac{\rho(\mathbf{r})\rho(\mathbf{r}')}{\mathbf{r}-\mathbf{r}'}\left[g(\mathbf{r},\mathbf{r}') - 1\right] d\mathbf{r}d\mathbf{r}' \tag{2.20}$$

where the first term corresponds to classical electrostatic interaction energy and second term contains the correlation effects. Since the electrons are fermions there is a spatial separation between the electrons with same spins due to antisymmetric wave function. This reduces the coulomb energy and this reduction is called exchange energy. Exchange energy can be included into the calculations via

Hartree-Fock approximation and the density and density matrix can be calculated from the Hartree-Fock ground state Slater determinant. Electrons with opposite spins are also spatially separated due to coulomb interaction. The correlation energy is the difference between the total energy of the system and calculated Hartree-Fock energy.

From equations 14 and 20 the electronic energy of the system can be written as:

$$E = T + V + \frac{1}{2}\int \frac{\rho(\mathbf{r})\rho(\mathbf{r}')}{\mathbf{r}-\mathbf{r}'} d\mathbf{r}d\mathbf{r}' + E_{XC} \tag{2.21}$$

and the kinetic energy and energy due to external field can be expressed as:

$$\begin{aligned} T &= \left\langle \Phi \left| -\frac{\hbar^2}{2m}\sum_{i=1}^{N}\nabla_i^2 \right| \Phi \right\rangle = -\frac{\hbar^2}{2m}\int \left[\nabla_{\mathbf{r}}^2 \rho_1(\mathbf{r},\mathbf{r}')\right]_{\mathbf{r}'=\mathbf{r}} d\mathbf{r} \\ V &= \sum_{I=1}^{P}\left\langle \Phi \left| \sum_{i=1}^{N} \upsilon(\mathbf{r}_i - \mathbf{R}_I) \right| \Phi \right\rangle = \sum_{I=1}^{P}\int \rho(\mathbf{r})\upsilon(\mathbf{r}-\mathbf{R}_I)d\mathbf{r} \end{aligned} \tag{2.22}$$

and E_{XC} is the exchange-correlation energy.

$$E_{XC} = \frac{1}{2}\int \frac{\rho(\mathbf{r})\rho(\mathbf{r}')}{|\mathbf{r}-\mathbf{r}'|}\left[g(\mathbf{r},\mathbf{r}')-1\right] d\mathbf{r}d\mathbf{r}' \tag{2.23}$$

2.4.1 Thomas-Fermi Theory

For the first time in 1927 Thomas and Fermi proposed that the total energy can be written in terms of the electronic density [7]. The theory is the crude model of the today's Density Functional Theory such that it did not include the exchange and correlation effects. By neglecting the E_{XC} in Eq. 2.21, the Thomas-Fermi total energy given as:

$$E_{TF}[\rho] = C_k \int \rho(\mathbf{r})^{5/3} d\mathbf{r} + \int \upsilon(\mathbf{r})\rho(\mathbf{r})d\mathbf{r} + \frac{1}{2}\int\int \frac{\rho(\mathbf{r})\rho(\mathbf{r}')}{|\mathbf{r}-\mathbf{r}'|} d\mathbf{r}d\mathbf{r}' \tag{2.24}$$

where the first term represents the kinetic energy and it can be calculated from the kinetic energy density of homogenous gas. Here C_k is equal to $3(3\pi^2)^{2/3}/10$. Thomas-Fermi total energy is depends only the electronic density and it is a functional of the density. By considering the constraint $\int \rho(\mathbf{r})d\mathbf{r} = N$ the total energy can be calculated from Eq. 2.24 variationally. In terms of functionals:

$$\frac{\delta}{\delta\rho(\mathbf{r})}\left[E_{TF}[\rho] - \mu\int \rho(\mathbf{r})d\mathbf{r}\right] = 0 \tag{2.25}$$

and the chemical potential (μ) is:

$$\mu = \frac{5}{3}C_k\rho(\mathbf{r})^{2/3} + \upsilon(\mathbf{r}) + \int \frac{\rho(\mathbf{r}')}{|\mathbf{r}-\mathbf{r}'|}d\mathbf{r} \tag{2.26}$$

This equation can be inverted to obtain the density as a *unique* function of the external potential.

2.4.2 Hohenberg-Kohn Theorem

In 1964, Hohenberg and Kohn proved that the total energy is a unique functional of the electron density [8]. First, they showed that the potential is univocally determined by the electronic density. Let us assume two different potential can be generated by same electronic density such that two potentials ν and ν' corresponds to same $\rho(r)$. E_0, ψ are the ground state energy and ground state of H, and E_0', ψ' are the ground state energy and ground state of H'. According to variational principle:

$$E_0 < \langle\psi'|H|\psi'\rangle = \langle\psi'|H'|\psi'\rangle + \langle\psi'|H-H'|\psi'\rangle = E_0' + \int \rho(\mathbf{r})(\nu(\mathbf{r})-\nu'(\mathbf{r}))d\mathbf{r} \tag{2.27}$$

with same treatment:

$$E_0' < \langle\psi|H'|\psi\rangle = \langle\psi|H|\psi\rangle + \langle\psi|H'-H|\psi\rangle = E_0 - \int \rho(\mathbf{r})(\nu(\mathbf{r})-\nu'(\mathbf{r}))d\mathbf{r} \tag{2.28}$$

Combining equations 2.27 and 2.28 gives $E_0 + E_0' < E_0' + E_0$, so that our assumption is wrong and $\nu(\mathbf{r})$ and $\nu'(\mathbf{r})$ should be same except for a trivial additive constant.

Since ground state wave function is determined by the potential, it is also functional of the electronic density.

The second theorem of Hohenberg and Kohn is $E_0 < E_\nu[\tilde{\rho}]$ where $\tilde{\rho}(r)$ is the electronic density normalized to N. And $E_\nu[\tilde{\rho}]$ is:

$$E_\nu[\tilde{\rho}] = F[\tilde{\rho}] + \int \tilde{\rho}(\mathbf{r})\nu(\mathbf{r})d\mathbf{r} \tag{2.29}$$

where $F[\tilde{\rho}]$ is:

$$F[\tilde{\rho}] = \langle \psi[\tilde{\rho}] | T + V | \psi[\tilde{\rho}] \rangle \tag{2.30}$$

The proof is simple. Due to variational principle:

$$\langle \psi[\tilde{\rho}] | H | \psi[\tilde{\rho}] \rangle = F[\tilde{\rho}] + \int \tilde{\rho}(\mathbf{r}) \nu(\mathbf{r}) d\mathbf{r} = E_\nu[\tilde{\rho}] \geq E_\nu[\rho] = E_0 = \langle \psi | H | \psi \rangle \tag{2.31}$$

Then;

$$\delta \left\{ E_\nu[\rho] - \mu \left(\int \rho(\mathbf{r}) d\mathbf{r} - N \right) \right\} = 0 \tag{2.32}$$

which implies generalized Thomas-Fermi equation;

$$\mu = \frac{\delta E_\nu[\rho]}{\delta \rho} = \nu(\mathbf{r}) + \frac{\delta F[\rho]}{\delta \rho} \tag{2.33}$$

These two theorems are the fundamental theorems of the Density Functional Theory (DFT). Here $F[\rho]$ is a universal functional of the electronic density.

2.4.3 Kohn-Sham Energy Functional

In 1965 Kohn and Sham showed that the total energy of a system can be calculated by self-consistent one-electron equations [9]. After successive iterations the minimum value of the energy gives the ground state energy of the system. The total energy is:

$$E\left[\Phi_i\right] = 2 \sum_i \int \Phi_i \left[-\frac{\hbar^2}{2m} \right] \nabla^2 \Phi_i d\mathbf{r} + \int V_{ext} \rho(\mathbf{r}) d\mathbf{r} + \frac{e^2}{2} \int \frac{\rho(\mathbf{r}) \rho(\mathbf{r}')}{|\mathbf{r} - \mathbf{r}'|} d\mathbf{r} d\mathbf{r}' + E_{XC}\left[\rho(\mathbf{r})\right] \tag{2.34}$$

Electronic density can be calculated by:

$$\rho(\mathbf{r}) = 2 \sum_i |\Phi_i(\mathbf{r})|^2 \tag{2.35}$$

where 2 comes from the sum of the spin states. The minimum of the above functional gives the ground state energy of the system.

2.4.4 Kohn-Sham Equations

To calculate the set of wave functions, $\Phi_i(\mathbf{r})$, that minimizes the energy functional we can use the self-consistent solutions of the Kohn-Sham equations:

$$\left[-\frac{\hbar^2}{2m}\nabla^2 + V_{ext}(\mathbf{r}) + V_H(\mathbf{r}) + V_{XC}(\mathbf{r})\right]\Phi_i(\mathbf{r}) = \varepsilon_i\Phi_i(\mathbf{r}) \tag{2.36}$$

where V_H is the Hartree potential and given as:

$$V_H(\mathbf{r}) = e^2\int\frac{\rho(\mathbf{r}')}{|\mathbf{r}-\mathbf{r}'|}d\mathbf{r}' \tag{2.37}$$

and V_{XC} is the exchange-correlation potential given by:

$$V_{XC}(\mathbf{r}) = \frac{\delta E_{XC}\left[\rho(\mathbf{r})\right]}{\delta\rho(\mathbf{r})} \tag{2.38}$$

The importance of the Kohn-Sham equations is they reduces the many-electron system to non-interacting electrons system in which the electrons are moving in an effective potential due to other electrons. The main difference between Kohn-Sham and Hartree-Fock approaches is effective potential in single-particle Schrödinger equations of Kohn-Sham contains exchange-correlation term. After creating reasonable charge density the equations can be solved and wave functions, V_H and V_{XC} can be found. Then after calculation of new charge density the new iteration can be performed. After enough successive iterations the minimum of the energy functional can be found. The total energy is the sum of single-particle Kohn-Sham eigenvalues but the double counting terms in the Hartree energy and exchange-correlation energy have to be subtracted. In fact the Kohn-Sham eigenvalues are not, strictly speaking the energies of the single-particle electron states, but rather the derivatives of the total energy with respect to the occupation numbers of these states. Nevertheless, the highest occupied eigenvalue in an atomic or molecular calculation is nearly the unrelaxed ionization energy for that system [1].

2.5 Local Density Approximation

Although Hohenberg-Kohn and Kohn-Sham theorems reduce many-particle Schrödinger equation into single-particle Schrödinger equations and provide that effective potential is a functional of electronic density, the exchange-correlation part is still problematic. The local density approximation assumes that the exhange-correlation potential is purely local. That is, the exchange-correlation energy can be written as the integral of charge density and local potential. Thus;

$$E_{XC}[\rho(\mathbf{r})] = \int \varepsilon(\mathbf{r})\rho(\mathbf{r})d\mathbf{r} \tag{2.39}$$

and

$$\frac{\delta E_{XC}[\rho(\mathbf{r})]}{\delta\rho(\mathbf{r})} = \frac{\partial[\rho(\mathbf{r})\varepsilon_{XC}(\mathbf{r})]}{\partial\rho(\mathbf{r})} \tag{2.40}$$

Furthermore, the exchange-correlation energy per electron at position $\mathbf{r}$ in inhomogeneous electronic system is equal to the exchange-correlation energy per electron in homogenous electron gas [1].

$$\varepsilon_{XC} = \varepsilon_{XC}^{hom}[\rho(\mathbf{r})] \tag{2.41}$$

Actually exchange-correlation energy is non-local due to nearby inhomogeneities in the electron density. The exchange-correlation energy density depends on the presence of other electrons in the surroundings of an electron at $\mathbf{r}$, through exchange-correlation hole. The local density approximation works so well in many cases because it gives the correct sum rule for the exchange-correlation hole [1]. Many of the other improvements, which tries to handle the exchange-correlation energy, do not work well as LDA just because they do not provide the correct sum rule.

Some important features of LDA are listed below [10]:

1. For homogenous system LDA works better. For systems where large deviations in the electronic density occurs the LDA tends to fail because the exchange-correlation energy becomes more non-local.

2. LDA gives larger binding energy of molecules and solids than correct value.

3. LDA predicts chemical trends, e.g. chemical bonds, well.

4. For covalent, ionic and metallic systems bond lengths, bond angles and phonon frequencies are well predicted by LDA whereas dieectric properties are overestimated by about an 10 percent error.

5. For weakly bound systems bond lengths are estimated too short.

In some circumstances LDA tends to fail. One of these is due to large deviations in electronic density which is given at above list. Moreover, in weak molecular bonds, the binding energy affected by inhomogeneities thus LDA approach is failed. Similarly, if the binding is due to charge-charge correlations (van der Waals type binding), the interaction is non-local. In addition, LDA fails to cancel the self-interaction so that in negatively charged ions LDA fails. Finally, energy gap in semiconductors calculated very small with LDA [10].

2.6 Generalized Gradient Approximation

The gradient expansion of the eletronic density, $\rho(\mathbf{r})$, which can be used to represent the exchange-correlation energy, is widely used non-local extension of the LDA. The XC energy has gradient expansion as;

$$E_{XC}[\rho] = \int A_{xc}[\rho]\rho(\mathbf{r})^{4/3}d\mathbf{r} + \int C_{xc}[\rho]|\nabla\rho(\mathbf{r})|^2/\rho(\mathbf{r})^{4/3}d\mathbf{r} + ... \tag{2.42}$$

Thus the XC energy has the form;

$$E_{XC} = \int \rho(\mathbf{r})\varepsilon_{XC}[\rho(\mathbf{r})]d\mathbf{r} + \int F_{XC}[\rho(\mathbf{r}), \nabla\rho(\mathbf{r})]d\mathbf{r} \tag{2.43}$$

where F_{XC} shuld satisfy the formal conditions such that sum rules, long range decay, etc. Otherwise the GGA calculations results badly [10]. There are several exchange-correlations functionals developed by Langreth-Mehl [11], Perdew-Wang '86 [12], Perdew-Wang '91 [13], Becke '88 [14], etc. There are some improvements of GGA over LDA depending on the system. Binding energies, atomic energies, bond lengths and angles might be more accurate by using GGA in general. But, at the end, these are approximations, and exact forms are not known.

Several different functional forms (as given above) are fitted to quantum Monte Carlo solutions for homogenous electron gas. So, it is worthy to check which is better, LDA or GGA for real case.

2.7 Computational Details

In the preceeding sections we showed that many-particle Schrödinger equation can be reduced to single-particle Schrödinger equations in terms Kohn-Sham formulation and every component in the equations are the functionals of electronic density $\rho(\mathbf{r})$. Moreover we examined two different approaches to handle exchange-correlation energy. But in a crystal there are infinite number of ions and infinite number of non-interacting electrons moving in a effective potential so that infinite number of single-particle Schrödinger equations have to solved. In addition, every wave function extends over a entire crystal so that infinite number of basis set has to be used in computational calculation. To overcome these difficulties first I'll give the Bloch's theorem.

2.7.1 Bloch's Theorem

Bloch's theorem states that each wave electronic wave function in lattice can be chosen to have the form of a plane wave times a function with the periodicity of the lattice;

$$\psi(\mathbf{r}) = exp[i\mathbf{k}.\mathbf{r}]f_i(\mathbf{r}) \tag{2.44}$$

The periodic part $f_i(\mathbf{r})$ can be expanded in terms of plane wave basis sets such that;

$$f_i(\mathbf{r}) = \sum_{\mathbf{G}} c_{i,\mathbf{G}} exp[i\mathbf{G}.\mathbf{r}] \tag{2.45}$$

where $\mathbf{G}$ are the reciprocal lattice vectors which can be defined by $\mathbf{G}.\mathbf{l} = 2\pi m$ where l is a lattice vector and m is a integer. Thus Eq. 2.44 and Eq. 2.45 gives;

$$\psi_i(\mathbf{r}) = \sum_{\mathbf{G}} c_{i,\mathbf{k}+\mathbf{G}} exp[i(\mathbf{k}+\mathbf{G}).\mathbf{r}] \tag{2.46}$$

2.7.2 Plane-wave basis sets

In order to solve Kohn-Sham equations (Eq. 2.36), we can expand wave function in terms of some basis set. (e.g. if the basis set is atomic orbital the method is called Linear Combination of Atomic Orbital (LCAO) or tight binding). Since the potential is periodic inside crystal, plane waves are very convenient basis set. Thus, substitution of Bloch's theorem (Eq. 2.46) into Kohn-Sham equations (Eq. 2.36) and integration over $\mathbf{r}$ gives:

$$\sum_{\mathbf{G'}}[\frac{\hbar^2}{2m}|\mathbf{k}+\mathbf{G}|^2\delta_{\mathbf{GG'}} + V_{ion}(\mathbf{G}-\mathbf{G'}) + V_H(\mathbf{G}-\mathbf{G'}) + V_{XC}(\mathbf{G}-\mathbf{G'})]c_{i,\mathbf{k}+\mathbf{G'}} = \varepsilon_i c_{i,\mathbf{k}+\mathbf{G}} \quad (2.47)$$

where V_{ion}, V_H and V_{XC} are the Fourier transforms of the ion-ion, Hartree and exchange-correlation potentials. Thus, the total energy of the system in momentum-space (see Ihm *et al.* [15]) is:

$$E_{total} = \sum_i \epsilon_i - \frac{1}{2}\Omega\left[\sum_{\mathbf{G}} V_H(\mathbf{G})\rho(\mathbf{G}) + \frac{1}{4}\sum_{\mathbf{G}}\mu_{xc}(\mathbf{G})\rho(\mathbf{G})\right] + \frac{1}{2}\sum_{\mu,\nu,\mu\neq\nu}\frac{2Z^2}{|\mathbf{R}_\mu - \mathbf{R}_\nu|} \quad (2.48)$$

where Ω is the total volume of the solid, $\rho(\mathbf{G})$ is the Fourier transform of the density and μ_{xc} is:

$$E_{XC}(\mathbf{r}) = \int \mu_{xc}(\mathbf{r})d\rho(\mathbf{r}) \quad (2.49)$$

As seen from Eq. 2.47, kinetic energy is diagonal and the solution of the equation can be obtained by diagonalization of the Hamiltonian matrix. At first glance one can think that infinite number of plane-waves should be used so that the dimension of the secular equation will be infinite but plane waves with large kinetic energy $(\hbar^2/2m)[\mathbf{k}+\mathbf{G}]^2$ can be omitted because these high-energetic plane waves do not contribute significantly to the total energy. So some particular cutoff energy (E_{cutoff}) can be chosen and plane-wave basis set can be truncated at some particular point during the simulation and thus the dimensions of the matrix depends on the cutoff energy $(\hbar/2m)|\mathbf{k}+\mathbf{G}_c|^2$. Introduction of an energy cutoff to the discrete plane wave basis set produces a finite basis set.

It is obvious that the truncation of basis set will cause an error in the calculation, but this error can be reduced by choosing higher cutoff energies. In principle, the appropriate cutoff energy should be at least at the value where the convergence of total energy is attained. Moreover, the number of basis states changes discontinuously with cutoff energy. The error at this stage can be reduced by choosing denser **k** point mesh but the problem is still present. It is possible to add a correction factor which is the difference between the number of basis states with infinite number of **k** points and the number of basis states with **k** points used in the calculation [1].

2.7.3 Pseudopotential Approximation

Since the Coulomb potential inversely proportional with position (**r**), the valence electrons move in a strong ionic potential in the core region so that the wave functions of the valence electrons oscillate rapidly at that region. Thus very large number of plane-waves should be used to obtain desired convergence. The same is true for tightly bound core electrons. These oscillations maintain the orthogonality between the core wave functions and the valence wave functions. which is required by the Pauli exclusion principle [1]. The pseudopotential theory (for theoretical approach see Kaxiras [16]) is used to expand the valance electrons wave functions at the core regions with small number of plane-wave basis set.

Many of the physical properties depends on the valance electrons. Pseudopotential approximation removes the core electrons and consider the crystal as ions and valence electrons. It also replaces the strong ionic potential with weaker pseudopotential that acts on a set of pseudo wave functions rather than true wave functions. The Fig. 2.1 shows the schematic illustration of real and pseusopotentials, and corresponding wave functions. The pseudopotential is constructed, ideally, so that its scattering properties or phase shifts for the pseudo wave functions are identical to the scattering properties of the ion and the core electrons for the valence wave functions,but in such a way that the pseudo wave functions have no radial nodes in the core region. The phase shift produced by the ion

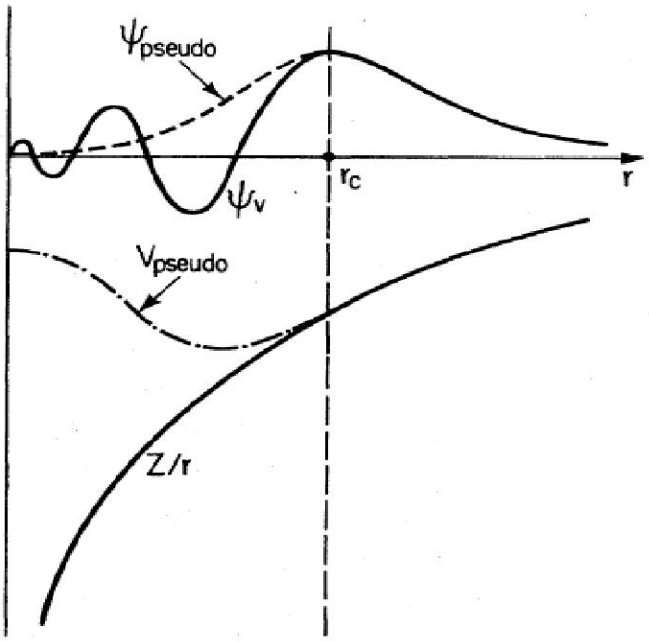

Figure 2.1: A schematic diagram of core potential, pseudopotential and corresponding wave functions. Above r_c these two potentials are same.

core is different for each angular momentum component of the valence wave function, and so the scattering from the pseudopotential must be angular momentum dependent. The general form of the pseudopotential is;

$$V_{NL} = \sum_{lm} |lm\rangle V_l \langle lm| \tag{2.50}$$

where $|lm\rangle$ is the spherical harmonics and V_l is the pseudopotential for the angular momentum l. Acting on the electronic wave function with this operator decomposes the wave function into spherical harmonics, each of which is then multiplied by the relevant pseudopotential V_l.

2.7.4 k-point sampling

In total energy calculations **k**-point integrations are required for all values of the wave-vector **k** inside a Brillouin zone. For example, in order to calculate the

electronic density the following quantities have to calculated.

$$\begin{aligned} \rho_{\mathbf{k}}(\mathbf{r}) &= \sum_{n,\epsilon_k^{(n)}<\epsilon_F} |\psi_{\mathbf{k}}^{(n)}|^2 \\ \rho(\mathbf{r}) &= \int \frac{d\mathbf{k}}{(2\pi)^3} \rho_{\mathbf{k}}(\mathbf{r}) \end{aligned} \tag{2.51}$$

The crystal symmetry can be used to decrease the summation over $\mathbf{k}$ values in the Brillouin zone by applying different symmetry operations to map a particular $\mathbf{k}$-point to number of equivalent points [16]. Thus, with very few number of $\mathbf{k}$-points the sum in Eq. 2.51 can be calculated.

In total energy calculations the chosen number of $\mathbf{k}$ points is an important parameter such that more dense meshes reduces the computational error but increases the convergence time and computational time. The appropriate number of $\mathbf{k}$ points can be determined by trying different meshes (See Fig. 4.1).

In the literature different kinds of methods are developed to create special sets of $\mathbf{k}$ points in the Brillouin zone (Chadi and Cohen [17]; Joannopoulos and Cohen [18]; Monkhorst and Pack [19]; Evarestov and Smirnov [20]). These methods can be used to calculate electronic states and thus the total energy of an insulator or semiconductor by using a very small number of $\mathbf{k}$ points. For metallic systems denser $\mathbf{k}$ point mesh should be used to obtain desired convergence.

Chapter 3

LITERATURE SURVEY

3.1 Introduction

Crystalline gold widely uses as a calibration standard due to its chemical inertness, large isothermal compressibility and structural phase stability over high pressures and high temperatures in experimental setups. Moreover gold crystal is available in pure form in nature and it has a simple face-centered cubic (fcc) structure [21]. That is why complete description of physical and chemical properties of gold should be known. There are several experimental and computational efforts have been made in order to obtain the equation of state (EOS), the elastic properties, structural phase transitions and the phonon frequencies in the literature.

3.2 Experimental Results for Gold

The idea of using gold (Au) as a primary calibration standard was first proposed by Jamieson *et al.* [21] in 1982. Heinz and Jeanloz [22] provided pressure-volume data at room temperature up to 70 GPa using x-ray diffraction through

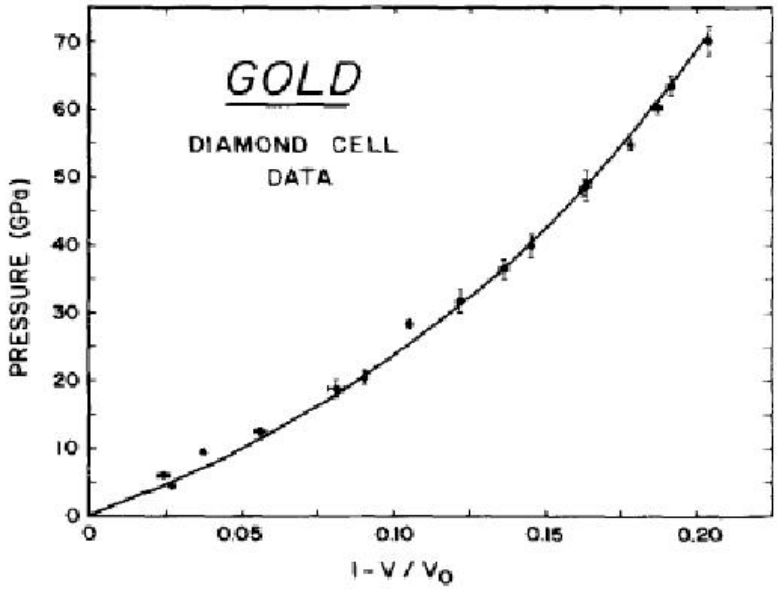

Figure 3.1: Heinz *et al.* [22] diamond-anvil cell data and Birch-Murnaghan [23][24][25] equation of state fit for Au.

a diamond-anvil cell and the ruby-fluorescence pressure scale. The bulk modulus and its derivative was found to be $K_T = 167$ ($\pm$ 11) GPa and $K'_T = 5.5$ ($\pm$ 0.8) GPa. Fig. 3.1 shows room-temperature static compression data and its Birch-Murnaghan fit. As seen from the figure their data were well fitted to Birch-Murnaghan [23][24][25] equation of state which is;

$$P = 3K_0 f(1+2f)^{5/2}(1-2\xi f) \tag{3.1}$$

where

$$\xi = (3/4)(K'_0 - 4) \tag{3.2}$$

and

$$f = (1/2)\left[\left(\frac{V_0}{V}\right)^{2/3} - 1\right] \tag{3.3}$$

Moreover they provided the Hugoniot data and derived the thermal equation of state for gold up to 200 GPa pressure and 3000 K temperature with the error in pressure about 1-2 percent. Thus gold can be used as a calibration standard in experiments performing in high pressures and high temperatures.

Golding *et al.* [26], measured the elastic constants of gold by ultrasonic pulse-superposition method at room temperature. Hiki *et al.* [27], and Daniels *et al.*

Table 3.1: Golding *et al.* [26], Hiki *et al.* [27] and Daniels *et al.* [28] results of zero-pressure elastic constants and pressure derivatives of Au. The elastic constants are in units of GPa.

c_{11}	c_{12}	c_{44}	$\partial c_{11}/\partial P$	$\partial c_{12}/\partial P$	$\partial c_{44}/\partial P$	B	ref
192.4	163.0	42.0	6.73	5.86	1.84	172.8	[26]
192.9	163.8	41.5	5.71	4.95	1.52	173.5	[27]
192.2	162.8	42.0	7.01	6.14	1.79	172.6	[28]

[28], measured same quantities using ultrasonic interference method and modified ultrasonic pulse-echo method, respectively. Table 3.1 shows the results of these papers.

Duffy *et al.* [30] measured the EOS and elastic properties of gold and rhenium up to 37 GPa pressure using a technique called energy-dispersive x-ray diffraction together with the theory describing lattice strains under hydrostatic compression. Their results will be examined in following chapters.

3.3 Computational Results for Gold

Godwal *et al.* [31] performed first theoretical calculations to obtain equation of state of gold using first-principle calculations. They used linear muffin-tin orbitals (LMTO) technique [36] and added approximate corrections coming from lattice vibrations and electronic excitations to the pressure. Fig. 3.2 shows the 0 K temperature equation of state of gold and its Vinet *et al.* [32][33][34], Dodson [35], and Birch [23] fits. The experimental data is slightly lower than Godwal *et al.* results so as seen from the figure, the Birch-Murnaghan equation of state agree most closely to the data. In the same paper the band populations and band partial pressures were calculated and it has seen that the pressure is dominated by the d band because in all compressions d band is nearly full ($n_d \sim 10$) so that 5d and 6s orbitals can be chosen as valance orbitals. Fig. 3.3 shows the band populations and band partial pressures of s, p, d, and f bands. Godwal *et al.* calculated the equilibrium volume, bulk modulus and pressure derivative of bulk modulus as $V_0 = 107.54$ a.u, $B_0 = 165$ GPa, and $B_0' = 6.4$ with relative

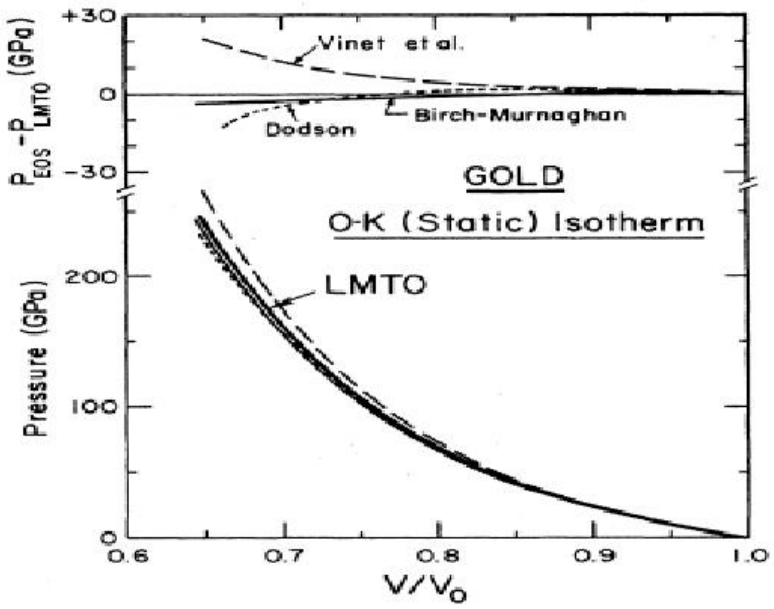

Figure 3.2: The equation of state of Au at 0 K obtained by Godwal *et al.* [31] using LMTO calculations. The heavy solid line is the calculated data, and other lines are the three equations of state: Vinet *et al.* [32][33][34], Dodson [35], and Birch [23]. Upper panel shows the pressure difference between these equations of state and LMTO calculations.

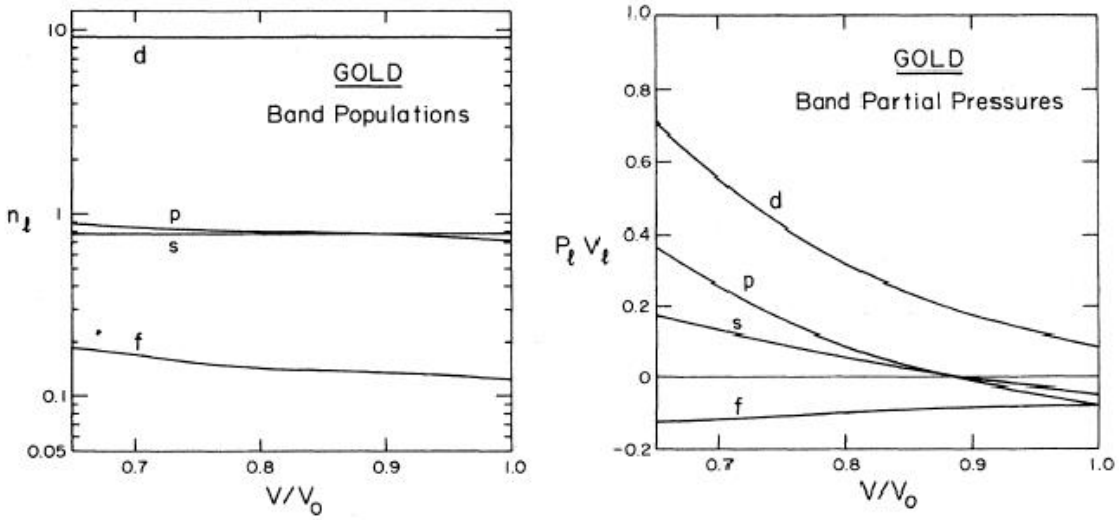

Figure 3.3: The figures show electron populations and partial pressured (in units rydbergs) for s, p, d, and f bands of gold as a function of relative volume, respectively. The calculations were based on LMTO method.

Table 3.2: Khein *et al.* [37] results of lattice constant and bulk modulus at equilibrium position using both LDA and GGA. The numbers inside the parenthesis shows the percentage error relative to experiment.

	LDA	GGA
a_0(a.u)	7.66(-0.1)	7.86(2.5)
B_0(GPa)	198(15.3)	142(-17.3)

Table 3.3: Tsuchiya *et al.* [40] findings of elastic constants and pressure derivatives for Au at zero-pressure using LDA. The elastic constant are in units of GPa.

c_{11}	c_{12}	c_{44}	$\partial c_{11}/\partial P$	$\partial c_{12}/\partial P$	$\partial c_{44}/\partial P$	C_s	B
201.3	176.1	36.9	5.97	5.38	1.43	12.6	184.5

errors 5.7, 0.8, and 17 percent respectively. Moreover they calculated the thermal equations of state at temperatures such that at 300K, 1000K, 2000K, and 3000K which were in agreement with experimental data.

Khein *et al.* [37] tested the accuracy of GGA over LDA for various materials such that Al, Ta, W, Pt, Cu, Ag, and Au. They used all-electron linearized-augmented-plane-wave method (LAPW) [38], and Perdew and Wang (PW91) [39] exchange-correlation functional for GGA. In all cases LDA predicted the lattice constant lower and bulk modulus larger than experimental value. For some materials GGA gave better results but for gold LDA predicted both lattice constant and bulk modulus better than GGA. Thus GGA does not give any improvement over LDA, The results of Khein *et al.* for gold are given in table 3.2.

The local density approximation (LDA) was first used by Tsuchiya *et al.* [40] in order to calculate equation of state and elastic properties of gold up to 100 GPa pressure using full-potential linear muffin-tin orbital (FP-LMTO) method [41]. The zero-pressure lattice constant, bulk modulus and pressure derivative, which were calculated by fitting the data to Birch-Murnaghan equation of state [23], were $a_0 = 4.066$ (Å), $B_0 = 176.1$ GPa and $B_0' = 6.1$ at 0 K temperature. The calculated elastic constants at zero-pressure are given in table 3.3.

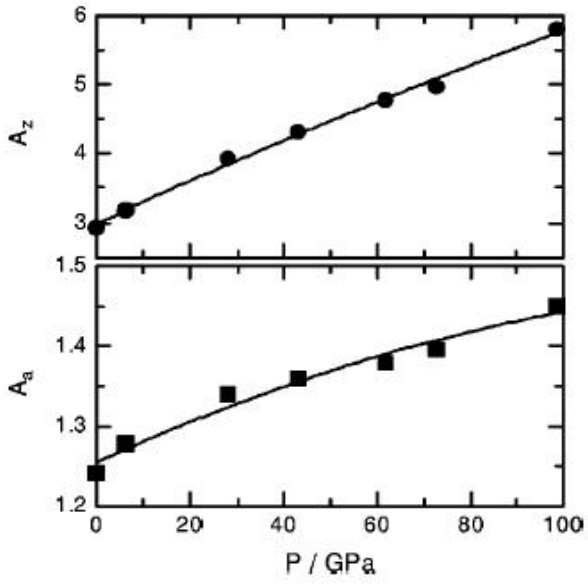

Figure 3.4: Two types of elastic anisotropy factor, the Zener ratio A_Z and acoustic anisotropy factor A_a. The figure is taken form Tsuchiya *et al.* [40]

The calculated elastic constants at higher pressures will be examined in Chapter 5 but here it should be noted that Au has small tetragonal shear constant (c_s) even at high pressures. This is mainly because of the small covalent contribution in chemical bonding of Au. Moreover the anisotropy of Au by means of two types of parameters, the Zener ratio and the acoustic anisotropy factor is obtained in the same paper. These ratios are defined as:

$$\begin{aligned} A_Z &= c_{44}/c_s \\ A_a &= (2c_{44} + c_{12})/c_{11} \end{aligned} \tag{3.4}$$

Their results at different pressures summarized in Fig. 3.4. As seen from the figure, Au has large anisotropy and it increases with pressure. Furthermore, Tsuchiya calculated the normalized elastic constants with respect to bulk modulus and saw that these parameters are insensitive to pressure.

Boettger [42] calculated the static-lattice equation of state and structural phase stability to 1 TPa pressure for both fcc, bcc and hcp structures using both LDA and GGA, and linear combinations of Gaussian-type-fitting-function

Table 3.4: Boettger's [42] results of equilibrium volume, bulk modulus and pressure derivative of bulk modulus. The LCGTO-FF method has been used. The table also shows the results with spin-orbit-coupling effects.

V_0 (a.u.)	B_0 (GPa)	B_0'	
111.36	1.90	5.1	LDA
110.60	1.92	5.1	LDA+SOC
120.87	1.42	5.5	GGA
119.95	1.45	5.4	GGA+SOC

(LCGTO-FF) method. Boettger observed that LDA model was a better approximation than GGA while performing zero-pressure calculations of Gold. For cubic structures calculations were performed with or without spin-orbit coupling (SOC) effects included. They concluded that spin-orbit coupling effects were negligible. Boettger obtained the static-lattice volume, bulk modulus and pressure derivative of bulk modulus, which are listed in table 3.3, by fitting the data with the stabilized jellium equation of state (SJEOS) of Alchagirov *et al.* [43] as;

$$\epsilon(x) = \frac{a}{x^3} + \frac{b}{x^2} + \frac{c}{x} + d \tag{3.5}$$

where

$$x = \left(\frac{V}{V_0}\right)^{1/3} \tag{3.6}$$

The terms in Eq. 3.5 corresponds to the energy contributions to the repulsive part of an electron-ion pseudopotential, the kinetic energy, Madelung and exchange energies, and correlation energy. Boettger observed that there is phase transition from fcc structure to hcp structure at 350 GPa and 410 GPa according LDA and GGA, respectively. There is no bcc stability observed at any pressure. The room-temperature calculations of Boettger agrees well with the experimental data.

Ahuja *et al.* [44] observed the fcc to hcp phase transition of gold using FP-LMTO method. $5s$, $5p$ bands were treated as pseudocore and $6s$, $6p$, $5d$, and $5f$ bands were treated as valence bands in the calculation. The transition pressures are 241 GPa for LDA and around 200 GPa for GGA. The hcp structure c/a ratio was optimized and found as c/a=1.63. Furthermore, Ahuja *et al.* tried to explain the reason of this transition and thus they calculated the density of states

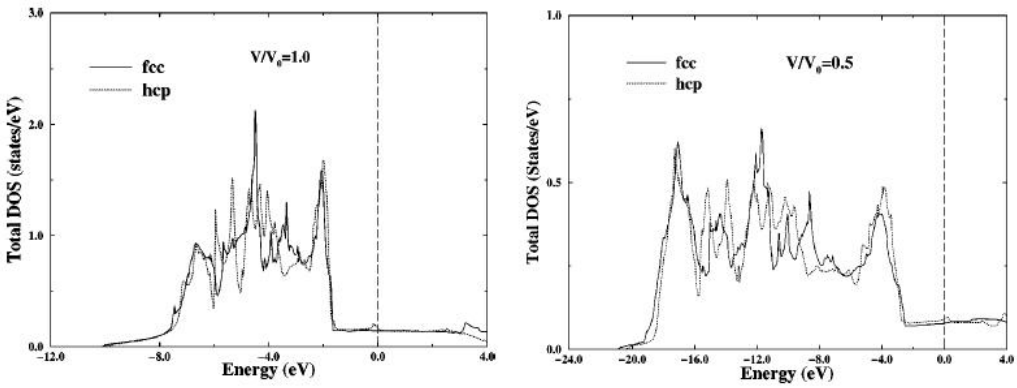

Figure 3.5: The figures shows the calculated density of states for fcc and hcp phases at two different volumes, $V/V_0 = 1.0$ and $V/V_0 = 0.5$. The figures are taken from Ahuja *et al.* [44]

(DOS) of gold for both fcc and hcp structures and for volumes $V/V_0 = 1.0$ and $V/V_0 = 0.5$. Fig. 3.5 shows the calculated DOS of gold for these volumes.

The DOS per eV at V/V_0=1.0 are 0.14 for fcc and 0.17 for hcp, and 0.08 and 0.09 for fcc and hcp at V/V_0=0.5, respectively. So Ahuja *et al.* concluded that the stability of hcp increasing over fcc with decreasing volume.

Söderlind [45] repeated the Ahuja *et al.* calculations for fcc, bcc, and hcp structures with considering the $5p$-$5d$ hybridization and found that bcc phase is more stable than hcp phase at high-pressures. Fig 3.6 shows the energy differences between hcp and bcc phases with respect to fcc phase. At 400 GPa there is phase transition from fcc to bcc.

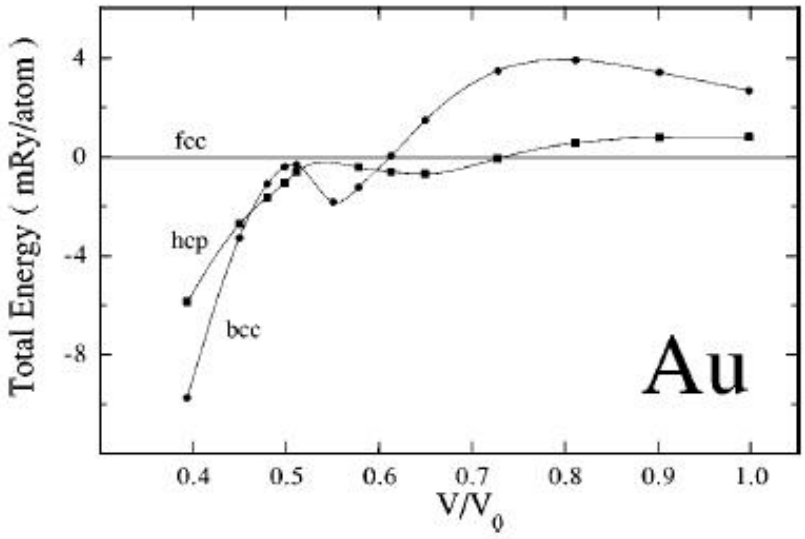

Figure 3.6: Söderlind [45] calculations is shown in order to demonstrate fcc-hcp-bcc structural phase transitions of Au.

Chapter 4

EQUATION OF STATE OF GOLD

4.1 Introduction

Gold in an important material such that it is used in high-pressure experiments as a calibration standard extensively. Thus equation of state and other physical properties of gold have particular importance. There are number of experimental studies were performed but these are limited to pressure ranges about 100 GPa. The EOS standard should be increased to higher pressures.

Although the accuracy of DFT electronic structure calculations is limited and cannot supply desired accuracy for EOS standard, such calculations do provide valuable qualitative guidance [42]. Firstly, the two most common approximations, local density approximation (LDA) and generalized gradient approximation (GGA), gives the upper and lower boundaries of the EOS. Moreover it is known that these two bounds converge to the correct value at ultrahigh pressure limit. Additionally the structural phases can be predicted well with both two models.

In this chapter, the results obtained from DFT electronic structure calculations for gold crystal is given. In sec 4.2 computational details are presented. In sec 4.3 EOS for gold with in LDA and GGA is investigated. In last section the structural phase transition of gold at ultrahigh pressures is discussed.

4.2 Computational Details

The calculations was performed using Vienna Ab-initio Simulation Package (VASP). Pseudopotential plane wave method [47] was used in DFT electronic structure calculations. Local density approximation and generalized gradient approximation (Perdew-Wang 91 type [39]) were used in order to express exchange-correlation potentials. The ultrasoft Vanderbilt pseudopotentials [48] were used in the calculations. $5d$ and $6s$ bands are treated as valence bands. Fig. 4.1 shows the energy cutoff test for plane waves at equilibrium lattice constant. So that the energy cutoff for plane waves is chosen to be 400 eV. The k-point sampling in the Brillouin zone (BZ) was modelled using Monkhorst-Pack [19] scheme. For the fcc and bcc phases 23x23x23 BZ mesh for all lattice dimensions was used. As seen from Fig. 4.2, which shows a typical k-point test, 23x23x23 mesh is appropriate for calculations. A comparable BZ meshes, which produce the same accuracy, were used for hcp structure depending on c/a ratio. Throughout calculations c/a ratios were optimized for every lattice constant. In order to treat the partial occupancy around the Fermi level of metallic system, the Fermi smearing of 0.08 eV is used in the calculations. The energy was converged within 10^{-4} eV/atom.

4.3 Results for Gold Crystal

The static-lattice DFT calculations were performed for gold crystal for various lattice parameters using LDA and GGA for fcc phase. The lattice parameter dependency of cohesive energy per atom is given in Fig. 4.3. The LDA approximation overestimated the cohesive energies as expected. The minimum of the energy curves in Fig. 4.3 determines the equilibrium volume (V_0) and cohesive energy (E_c). The discussion of results of this part is postponed to latter parts for conventional purposes.

Additionally, all calculations were carried out for fcc phase with spin polarization (SP) included. The results with SP effects were similar with previous calculations (without SP). The order of magnitude of energy differences between

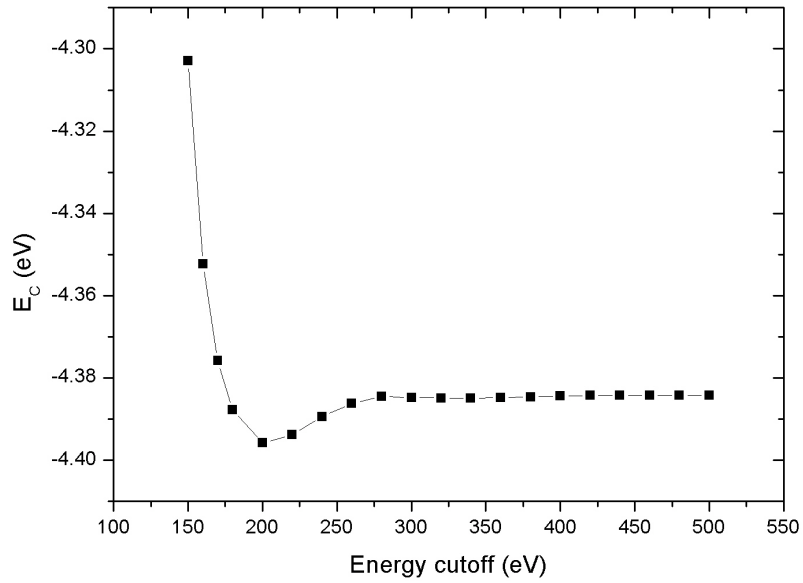

Figure 4.1: The test to determine the energy cutoff for plane waves.

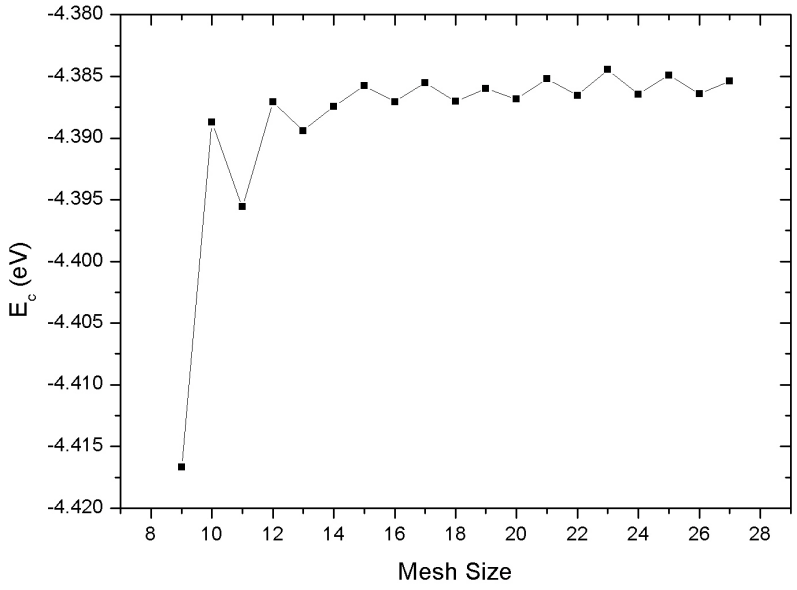

Figure 4.2: An example of k-point test.

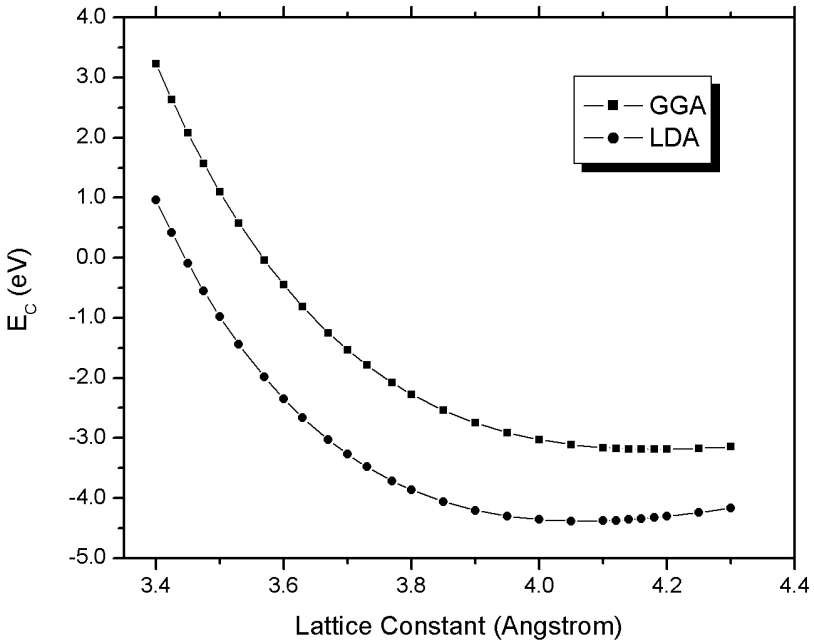

Figure 4.3: The variation of cohesive energy per atom with lattice constant a_0. Both LDA and GGA results are shown.

these calculations were in computational error range. Thus, spin-unpolarized calculations can be used. The main reason of this situation is there is no spin polarization at any direction because $5d$ orbital is fully occupied for gold atom. Moreover, it is shown that spin-orbit coupling effects are negligible by Boettger [42].

Fig. 4.4 shows the obtained equation of state of gold. Vinet [34] type of EOS based on both LDA and GGA results, and Heinz *et al.* [22] and Duffy *et al.* [30] experimental data are also shown in the figure. The EOS by using LDA is in agreement with experiment. The small discrepancy is mainly due to variation in equilibrium volumes, that is GGA and LDA are over and under estimating the zero-pressure volumes, respectively. At this point, it is useful to figure out the variation of pressure with respect to relative volume (see Fig. 4.5). As seen from the figure, LDA and GGA approximations predict upper and lower boundaries of the experimental data. Thus DFT calculations are capable of predicting the equation of state at ultra-high pressure regime.

After calculating the total energies at various volumes, the E-V data were analyzed in terms of different equations of states. Firstly energy expression (e.g. Eq. 4.1 and Eq. 4.2) was fitted and relevant parameters (such that equilibrium energy, volume and bulk modulus) were obtained, then by using these equation of state is calculated. The most common of these EOS's are Birch-Murnaghan (BM) [24] and Vinet [34] types. The BM formulation is;

$$\begin{aligned} E(V,T) &= E_0(T) + \frac{9B_0(T)V_0(T)}{8}\left\{1+\frac{\kappa}{2}(x^{-2}-1)\right\}(x^{-2}-1) \\ P(V,T) &= \frac{3}{2}B_0(T)\{x^{-7}-x^{-5}\}\left\{1+\frac{3}{4}\kappa(x^{-2}-1)\right\} \end{aligned} \tag{4.1}$$

where κ and x are;

$$\begin{aligned} \kappa &= B_0'(T) - 4 \\ x &= (V/V_0)^{1/3} \end{aligned} \tag{4.2}$$

Here B_0' is the pressure derivative of bulk modulus at zero-pressure. The Vinet type of EOS is;

Table 4.1: Equilibrium primitive cell volume, cohesive energy, bulk modulus and its pressure derivative are given for LDA and GGA approximations and two experimental data. The numbers in the parenthesis are the errors relative to Heinz-Jeanloz experimental data. Note that the values of last line calculated by analyzing the experimental data with BM EOS.

V_0 (Å^3)	E_0 (eV)	B (GPa)	$\partial B/\partial P$	ref
18.29 (7.8)	-3.19 (16)	134.16 (19.5)	5.97 (8.5)	GGA
16.82 (0.8)	-4.39 (15.6)	186.76 (12.1)	5.73 (4.18)	LDA
16.96	-3.796	166.65	5.5	Heinz-Jeanloz
16.95	...	170.65	4.72	Duffy

$$\begin{aligned} E(V,T) &= E_0(T) + \frac{9B_0(T)V_0(T)}{\xi^2}\{1 + \{\xi(1-x) - 1\}\exp\{\xi(1-x)\}\} \\ P(V,T) &= \left\{\frac{3B_0(T)(1-x)}{x^2}\right\}\exp\{\xi(1-x)\} \end{aligned} \tag{4.3}$$

where x is given in Eq. 4.2 and ξ is;

$$\xi = \frac{3}{2}(B_0' - 1) \tag{4.4}$$

The energy residues of these two types of EOS's from data is given in Fig. 4.6. As seen from the figure Vinet EOS is more preferable than BM EOS. This result is in contradiction with previous studies [31].

The zero-pressure primitive cell volume (V_0), cohesive energy (E_c), bulk modulus (B_0) and pressure derivative of bulk modulus ($\partial B/\partial P$) were obtained from the Vinet type EOS fit. Table 4.1 shows these obtained parameters and experimental data. From the table, it is seen that LDA overestimates higher bulk modulus and cohesive energy, and underestimates lattice parameter as expected.

To conclude the calculations with LDA results better than GGA. This is in agreement with previous computational studies [37][42].

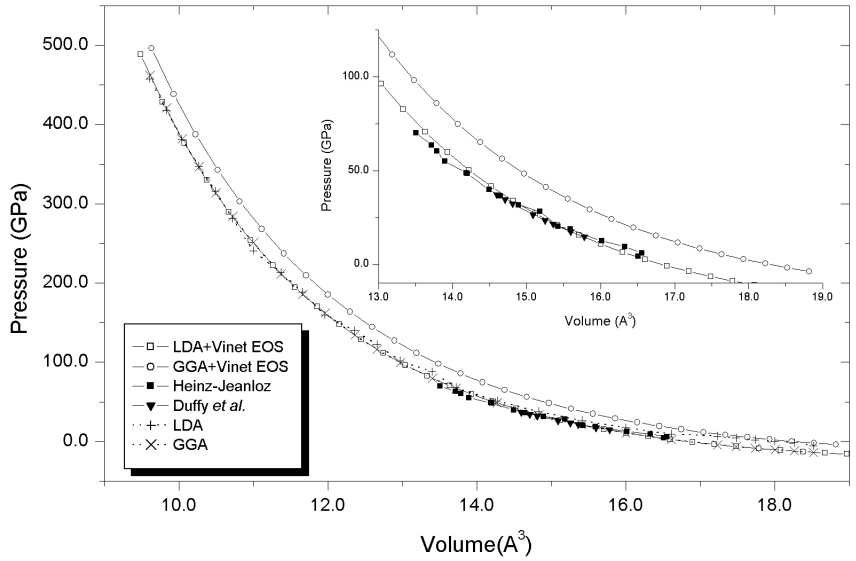

Figure 4.4: Equation of state of Au. Open symbols are the current results. Filled symbols are the experimental data of Heinz and Jeanloz [22] and Duffy *et al.* [30]. The output data are also shown for LDA and GGA. The small figure zooms to the 0-125 GPa pressure range.

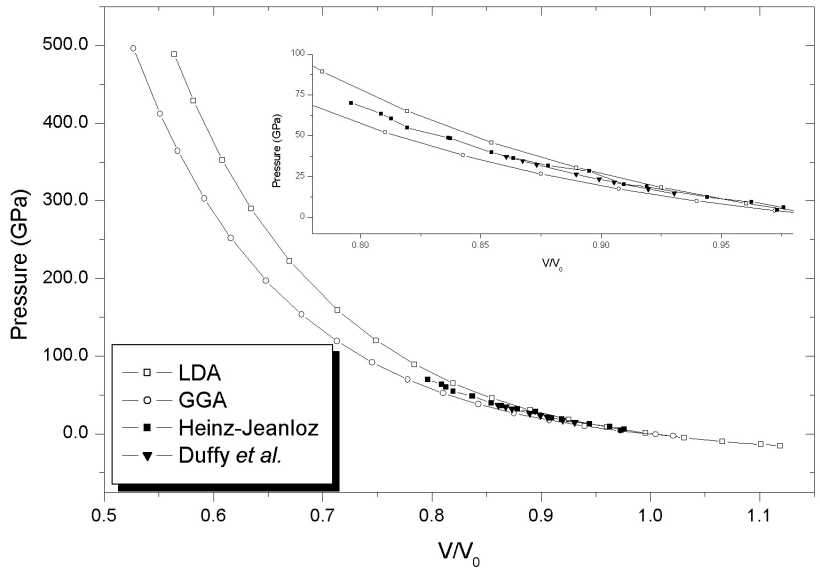

Figure 4.5: Pressure as a function of relative volume. Vinet EOS fits of LDA and GGA results are represented with open symbols. Two experimental data (Heinz-Jeanloz and Duffy) are also shown. The small figure shows the similar data at 0-100 Gpa pressure range.

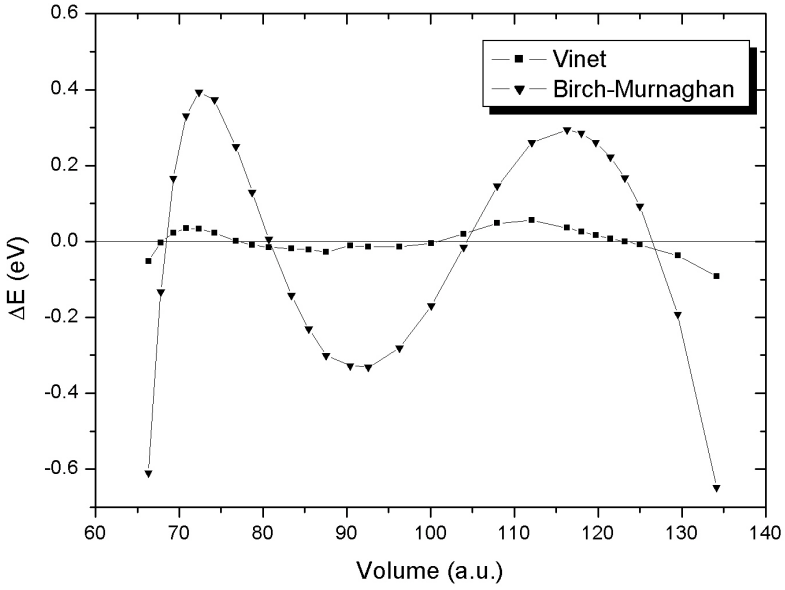

Figure 4.6: Variation of energy residues of Vinet and Birch-Murnaghan types of equation of states with respect to lattice volume.

4.4 Structural Phase Transition of Gold

The total energy DFT calculations were also performed for hcp and bcc structures of gold up to ultrahigh pressures. The accuracy of fcc and bcc structures were same since same k-point meshes were used at each lattice constant. The accuracy of hcp structure was obtained by choosing appropriate k-point mesh along z-direction consistent with c/a ratio. The c/a ratios was not taken as ideal but optimized at each volume. The energy differences of hcp and bcc phases relative to fcc phase with respect to volume is given in Fig. 4.4. The fcc phase is stable at zero-pressure and at low pressures. There is a phase transition from fcc phase to bcc phase at about 60% of the equilibrium volume. The transition pressures are 455 GPa (fcc to bcc) and 457 GPa (fcc to hcp) using LDA, 534 GPa (fcc to bcc) and 590 GPa (fcc to hcp) using GGA. Thus hcp phase stability was not observed. Transition volume is in agreement with previous studies [44] [42], but transition pressure is about 50% larger than previous study [42] (Furthermore, they claimed

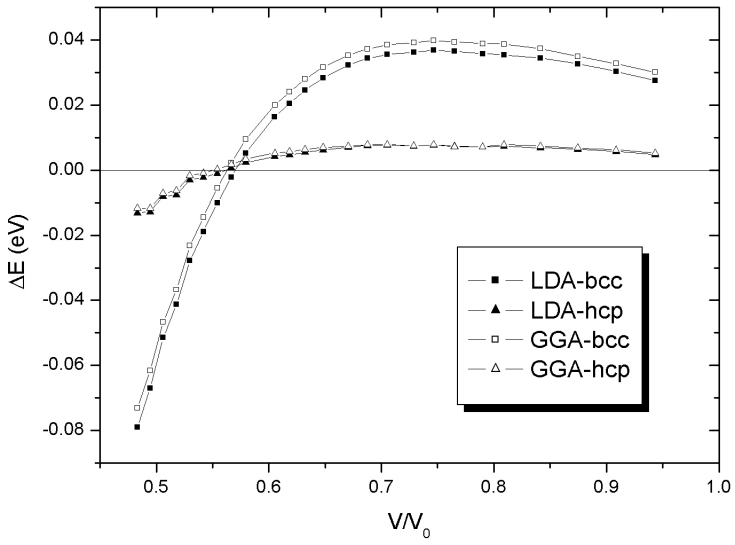

Figure 4.7: Energy difference between the bcc, hcp and the fcc structures. The fcc structure is used as the zero-energy reference level. The x-axis is the relative volume.

the fcc phase to hcp phase transition. This study is in better agreement with Söderlind's calculations [45]. The main reason of this discrepancy is, the pressure calculations at ultrahigh pressures results differently. Fig. 4.5 shows energy differences of hcp and bcc structures relative to fcc phase with respect to pressure for both LDA and GGA models.

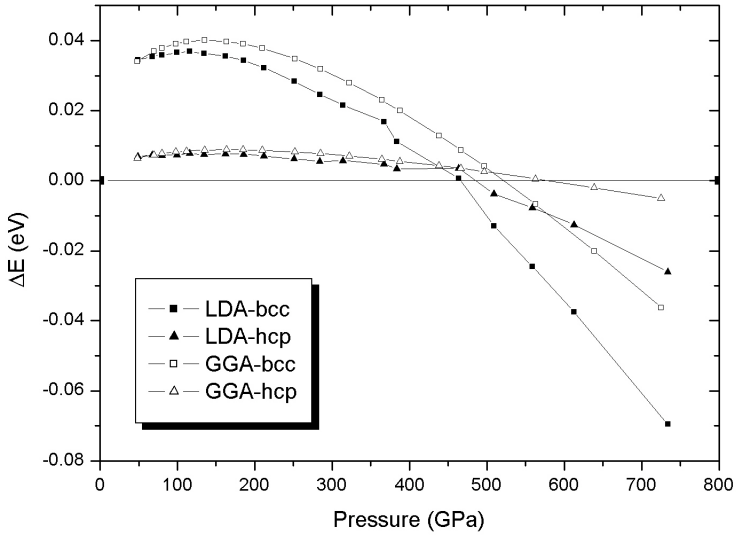

Figure 4.8: Energy differences between the bcc, hcp and the fcc structures for gold as a function of pressure. The fcc phase is used as the zero-energy reference level.

Chapter 5

ELASTIC PROPERTIES OF GOLD

The elastic constants of gold were calculated using DFT total energy calculations at 0-500 GPa pressure range. For cubic crystals there are only three independent stiffness constants due to high symmetry. In order to obtain c_{11}, c_{12} and c_{44} we applied three different deformations to fcc lattice. The bulk modulus at various pressures were obtained from EOS by applying the homogenous strain as in Eq. 5.1.

$$\epsilon = \begin{pmatrix} \delta/3 & 0 & 0 \\ 0 & \delta/3 & 0 \\ 0 & 0 & \delta/3 \end{pmatrix} \tag{5.1}$$

where δ is the deformation.

The tetragonal shear modulus (c_s) were calculated using the following strain, which is given at Eq. 5.2. Then the volume of the unit cell remains same but the unit cell becomes tetragonal.

$$\epsilon = \begin{pmatrix} \delta & 0 & 0 \\ 0 & \delta & 0 \\ 0 & 0 & (1+\delta)^{-2} - 1 \end{pmatrix} \tag{5.2}$$

The energy of the tetragonal cell for small deformations (δ) will be;

$$E(\delta) = E(0) + 6c_s V\delta^2 + O(\delta^3) \tag{5.3}$$

where *E(0)* is the total energy of the fcc phase, V is the volume of the unit cell.

The bulk modulus (B) and tetragonal shear modulus (c_s) are related with c_{11} and c_{12} such that;

$$\begin{aligned} B &= (c_{11} + 2c_{12})/3 \\ c_s &= (c_{11} - c_{12})/2 \end{aligned} \tag{5.4}$$

The third independent elastic stiffness constant (c_{44}) of a cubic crystal can be calculated from the strain as in Eq. 5.5. Again the volume of the unit cell remains same but it becomes orthorhombic.

$$\epsilon = \begin{pmatrix} 0 & \delta & 0 \\ \delta & 0 & 0 \\ 0 & 0 & \delta^2/(1-\delta^2) \end{pmatrix} \tag{5.5}$$

Then the energy of the orthorhombic cell is;

$$E(\delta) = E(0) + 2c_{44} V\delta^2 + O(\delta^4) \tag{5.6}$$

where the meanings of *E(0)* and V are similar to Eq. 5.3.

The zero-pressure elastic properties of gold crystal is given in table 5.1. Both LDA and GGA results are shown in the table and the references with asterisk are experimental results. The zero-pressure elastic constants using LDA are in better agreement with experimental results than GGA. Moreover, the LDA results tends to agree better with low temperature experimental data than ambient temperature data. The small discrepancies can be reduced by performing the calculations at experimental equilibrium lattice constant. The last line of the table shows the results at $a_0 = 4.06$ Å.

The pressure dependence of three elastic stiffness constants (c_{11}, c_{12} and c_{44}) is given in Fig. 5.1. The results of two computational work [46][40] and a experimental work [30] are also shown in the figure. Here our calculations were

Table 5.1: Elastic constants and pressure derivatives of three stiffness constants of Au at zero-pressure. LDA and GGA results and various experimental and computational data are given. The references with asterisk are the experimental studies. The units of elastic constants are GPa. The last line shows the LDA results at experimental equilibrium lattice constant.

ref	B	C_s	c_{11}	c_{12}	c_{44}	$\partial c_{11}/\partial P$	$\partial c_{12}/\partial P$	$\partial c_{44}/\partial P$
LDA	186.8	15.2	207.0	176.6	39.9	6.30	5.41	1.81
GGA	135.5	11.3	150.6	127.9	26.9	6.47	5.74	1.86
Daniels*	172.6	14.7	192.2	162.8	42.0	7.01	6.14	1.79
Hiki*	173.5	14.6	192.9	163.8	41.5	5.71	4.95	1.52
Golding*	172.8	14.7	192.4	163.0	42.0	6.73	5.86	1.84
Tsuchiya	184.5	12.6	201.3	176.1	36.9	5.97	5.38	1.43
Greeff	172.0	13.8	190.4	162.8	27.4	...	...	...
Duffy*	168.5	14.5	187.8	158.8	33.5	6.0	4.3	0.9
Biswas(79K)*	179.8	15.5	200.4	169.5	44.5	6.49	5.66	1.79
Biswas(298K)*	173.0	14.4	192.2	163.4	41.8	6.71	5.85	1.83
Anderson(0K)	180.3	16.0	201.6	169.7	45.4	...	...	...
Anderson(298K)	172.9	14.6	192.3	163.1	42.0	...	...	...
LDA @ exp	178.0	14.5	197.2	168.3	37.1	...	...	...

performed using LDA because equation of state calculations in chapter 4 and zero-pressure elastic constants calculations shows that LDA gives more accurate results. The current results are in agreement with computational results but slightly higher than experiment due to thermal effects which were not taken into consideration during the calculations. However, the thermal energy may soften the elastic constant and as a result improving the accuracy of calculations [40].

Fig. 5.2 and Fig. 5.3 shows the pressure dependence of tetragonal shear modulus and bulk modulus, respectively. Tetragonal shear modulus is in better agreement with experiment than previous studies and moreover it seems to give more accurate results at higher pressures. The tetragonal shear modulus c_S is small relative to c_{11} and c_{12}. This characteristic feature of gold crystal was explained by Söderlind *et al.* [53] such that the energy difference between fcc and bcc phases determines the c_S.

The effective bulk modulus B_{eff} and shear modulus G_{eff} can be determined from Voigt [49] and Reuss [50] approaches. Voigt assumed that the strain is uniform throughout the sample and Reuss assumed a uniform stress in the sample [51]. For both approaches the bulk modulus is same and given as;

$$B_{eff} = B_V = B_R = (c_{11} + 2c_{12})/3 \tag{5.7}$$

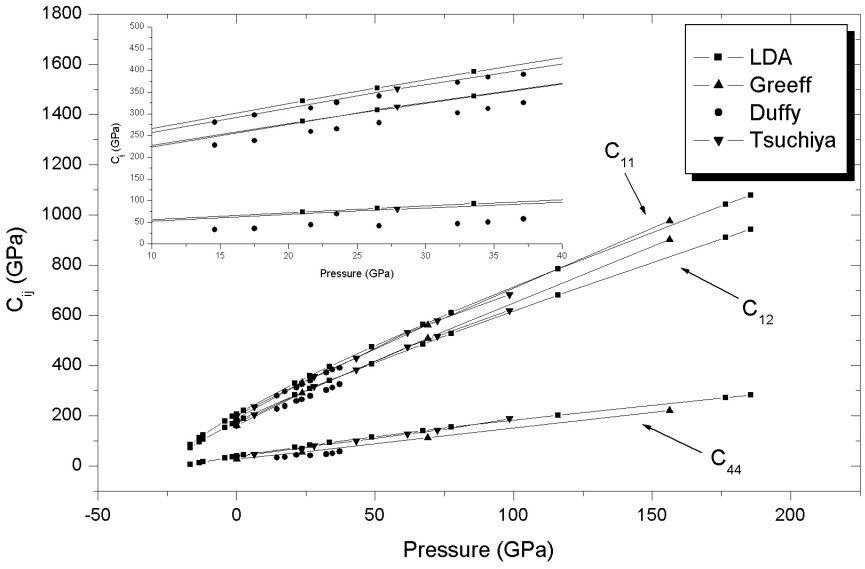

Figure 5.1: Static elastic constants of Au as a function of pressure. Filled squares are the calculated values, filled circles are the x-ray diffraction data of Duffy *et al.* [30], and filled triangles are the DFT calculations of Greeff [46] and Tsuchiya [40]. The figure inside shows the same physical quantities at 10-40 GPa pressure range.

Voigt averaged G_V and Reuss averaged G_R shear modulus are given as;

$$\begin{aligned} G_V &= (c_{11} - c_{12} + 3c_{44})/5 \\ G_R &= 5(c_{11} - c_{12})c_{44}/[4c_{44} + 3(c_{11} - c_{12})] \end{aligned} \tag{5.8}$$

Voigt and Reuss approaches are the lower and upper bounds to B and G for any crystal structure [52]. Thus;

$$\begin{aligned} B_R \leq B_{eff} \leq B_V \\ G_R \leq G_{eff} \leq G_V \end{aligned} \tag{5.9}$$

The zero-pressure averaged shear modulus are given in table 5.2. G_{VRH} is $(G_V + G_R)/2$. The results are in perfect agreement with experimental data.

The elastic anisotropy of Au was investigated in terms of Zener ratio [27] which is given as;

$$A_Z = 2c_{44}/(c_{11} - c_{12}) = c_{44}/c_S \tag{5.10}$$

Table 5.2: Zero-pressure Voigt [49] (assumes uniform strain) and Reuss [50] (assumes uniform stress) assumptions of averaged shear modulus. G_{VRH}=$(G_V + G_R)/2$. All shear modulus have the units of GPa. The references with asterisk are the experimental works. The last line shows the LDA calculation at experimental equilibrium lattice constant.

ref	G_V	G_R	G_{VRH}
LDA	30.0	24.2	27.1
GGA	20.8	17.6	19.1
Daniels*	31.1	24.1	27.6
Hiki*	30.7	23.8	27.3
Golding*	31.1	24.1	27.6
Tsuchiya	27.2	20.8	24.0
Greeff	22.0	19.7	20.8
Duffy*	25.9	21.9	23.9
Biswas(79K)*	32.9	25.4	29.1
Biswas(298K)*	30.8	23.7	27.3
Anderson(0K)	33.6	26.1	29.9
Anderson(298K)	31.0	24.0	27.5
LDA @ exp	28.1	22.9	25.5

The pressure dependence of anisotropy of Au is given in Fig. 5.4. At zero pressure the anisotropy is 2.62 and increases slightly with pressure. This result is expected since pressure dependence of elastic constant c_{44} is higher than tetragonal shear modulus c_S.

The sound velocities can be determined by solving the Christoffel equation [54]:

$$(c_{ijkl} n_j n_k - \rho \nu^2 \delta_{ij}) u_i = 0 \tag{5.11}$$

where c_{ijkl} is the elastic constants tensor, $\overrightarrow{n}$ is the propagation direction, $\overrightarrow{u}$ is the polarization vector, ρ is the mass density and ν is the velocity. For cubic crystals, the solution of the secular equation (Eq. 5.) is simple and for [110] direction the longitudinal mode is

$$\rho \nu^2 = (c_{11} + c_{12} + 2c_{44})/2 \tag{5.12}$$

and two transverse modes are

$$\begin{aligned} \rho \nu^2 &= c_{44} \\ \rho \nu^2 &= (c_{11} - c_{12})/2 \end{aligned} \tag{5.13}$$

polarized along [001] and $[1\bar{1}0]$ directions. The compressional, shear and bulk sound velocities are related with bulk modulus and G_{VRH} such that

$$\nu_P = [(B + 4/3G)/\rho]^{1/2}$$

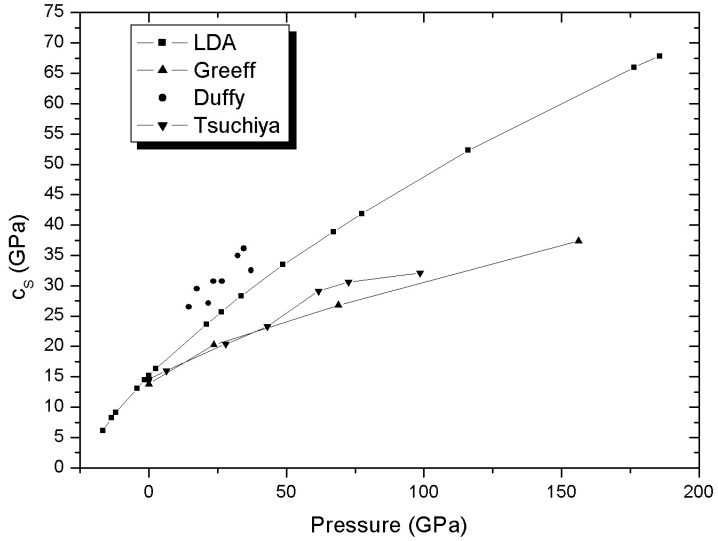

Figure 5.2: Variation of tetragonal shear modulus, c_S, with pressure. Filled squares are the current results. Filled circles are the experimental data of Duffy *et al.* [30], filled triangles are the computational data of Greeff [46] and Tsuchiya [40].

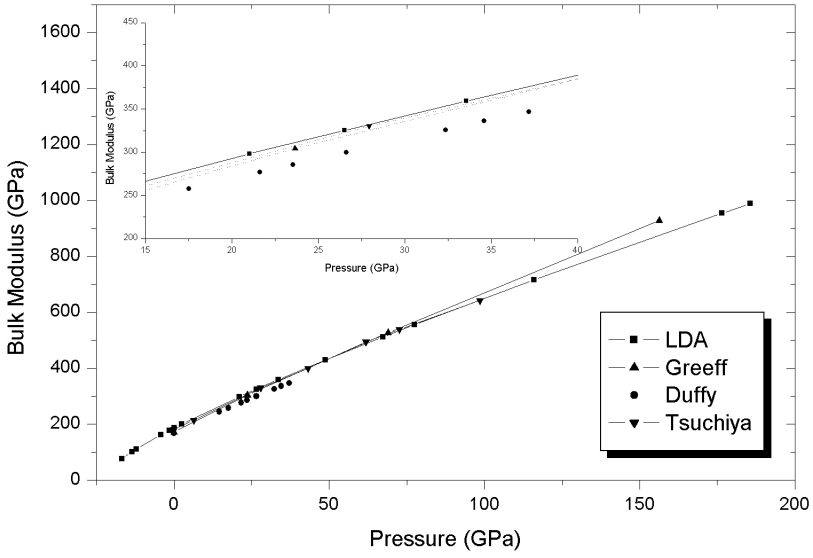

Figure 5.3: Pressure dependence of bulk modulus. The small figure shows the same quantities at 200-450 GPa pressure range. An experimental data (Duffy *et al.* [30] and two computational data (Greeff [46], Tsuchiya [40])are also shown in figure.

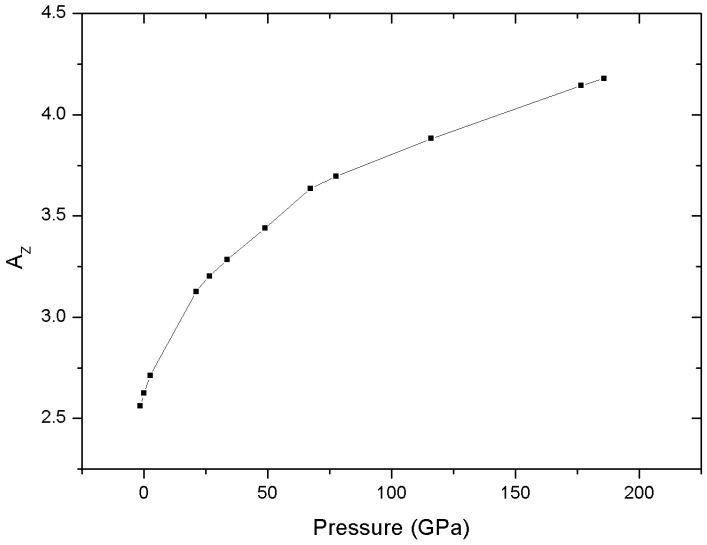

Figure 5.4: Pressure dependence of elastic anisotropy, A_Z.

$$\begin{aligned} \nu_S &= (G_{VRH}/\rho)^{1/2} \\ \nu_B &= (B/\rho)^{1/2} \end{aligned} \tag{5.14}$$

The sound velocities calculated from elastic constants are shown in Fig. 5.5.

The band structures and density of states of fcc phase at 0, 200 and 600 GPa pressures are shown in figures 5.6, 5.7 and 5.8, respectively. Figures 5.9 and 5.9 shows the band structures (with density of states) of bcc Au at zero and 600 GPa pressures. The d-bands are almost full and s-bands cross the fermi levels. The partially full s-bands are responsible for the conductivity of gold.

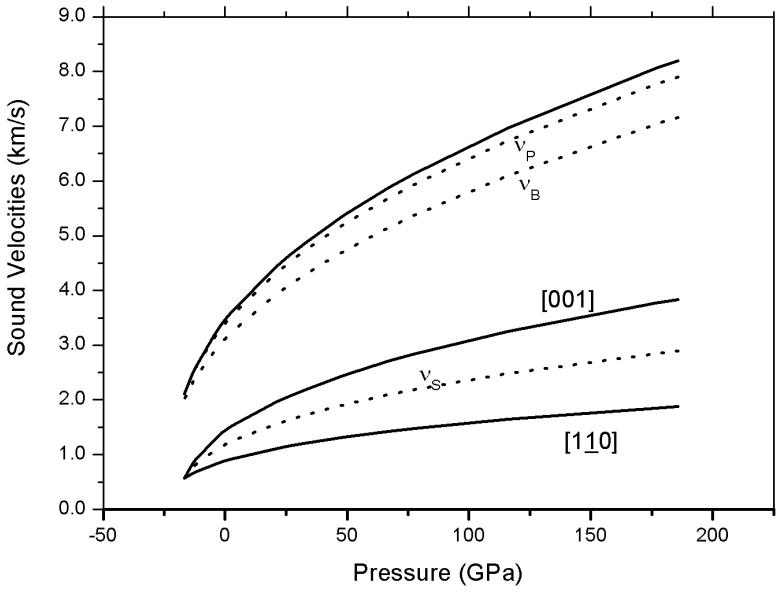

Figure 5.5: Sound velocities of Au as a function of pressure. Solid lines are two transverse and one longitudinal sound velocities along [110] direction. Brackets indicates the polarization directions. Dotted lines are the isotropic aggregate velocities, ν_P, ν_S, and ν_B.

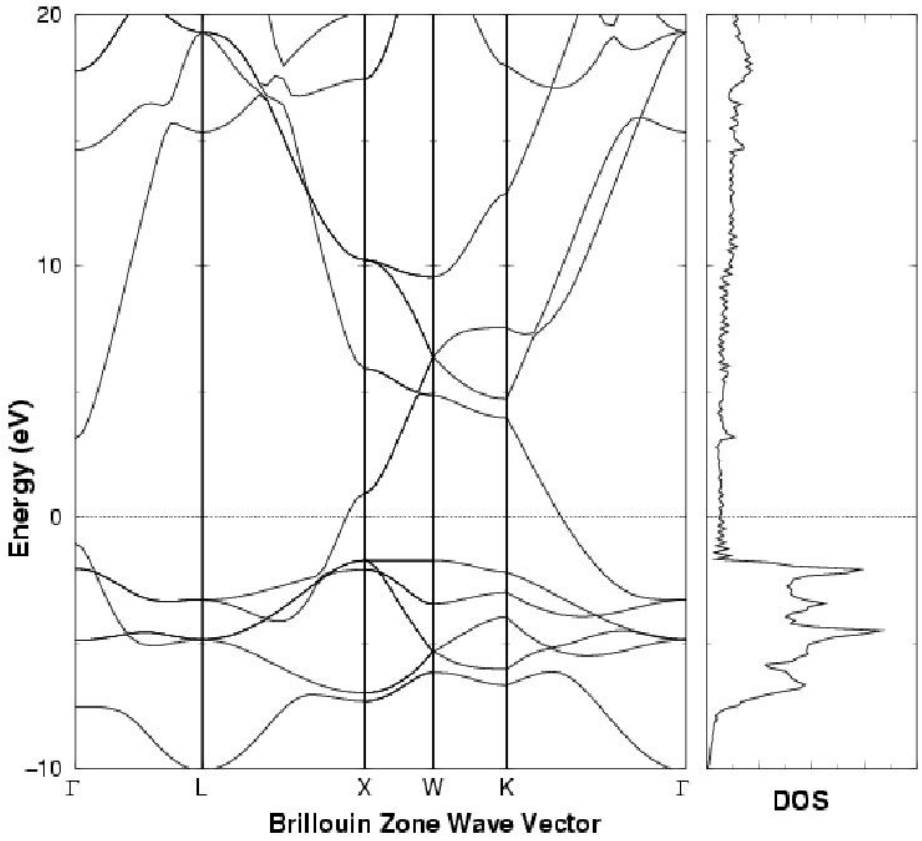

Figure 5.6: Scalar relativistic LDA electronic band structure and density of states for fcc Au at zero pressure. The energies are given relative to the Fermi level, the dotted line.

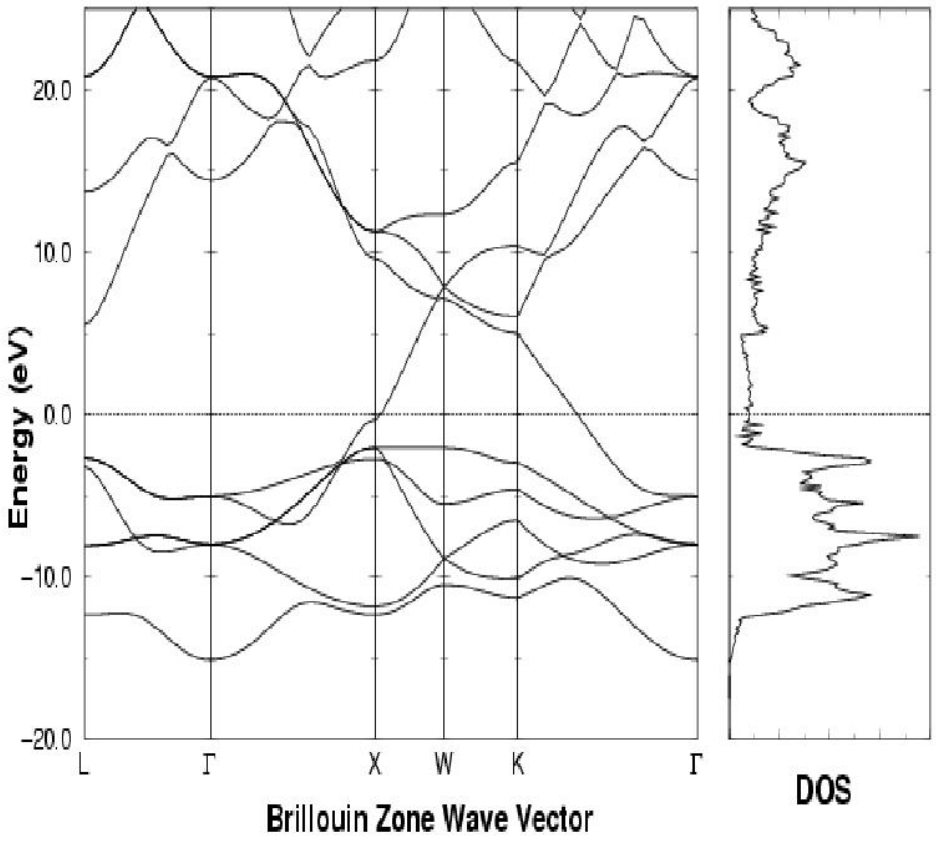

Figure 5.7: Scalar relativistic LDA electronic band structure and density of states for fcc Au at 200 GPa pressure. The energies are given relative to the Fermi level, the dotted line.

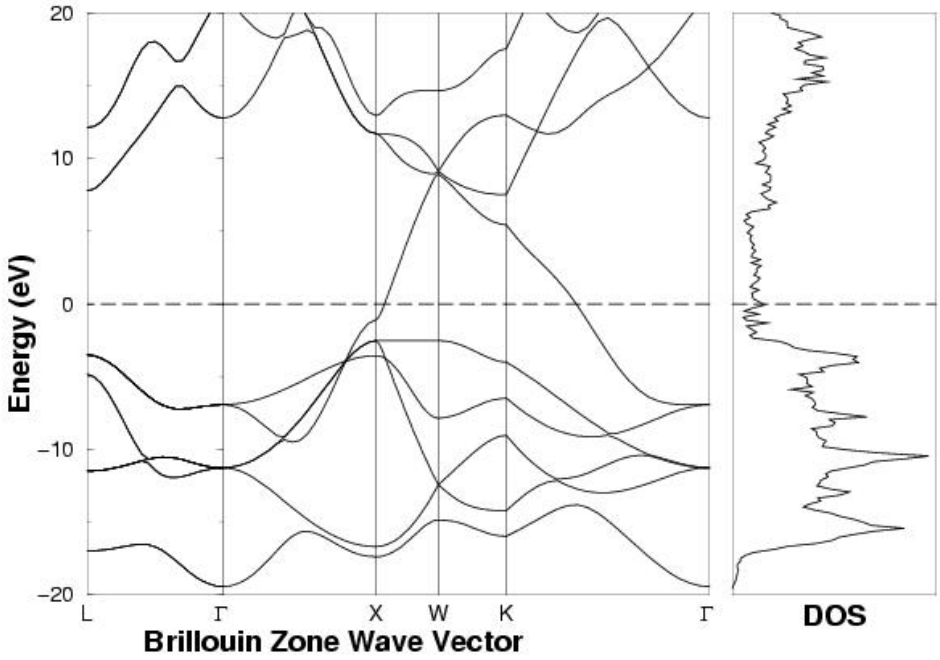

Figure 5.8: Scalar relativistic LDA electronic band structure and density of states for fcc Au at 600 GPa pressure. The energies are given relative to the Fermi level, the dotted line.

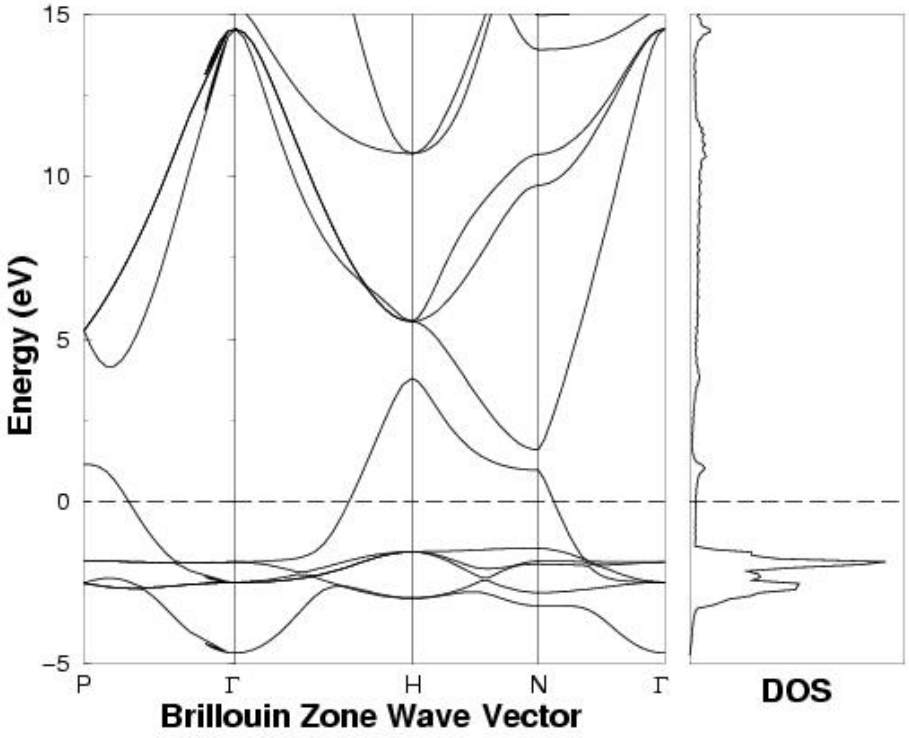

Figure 5.9: Scalar relativistic LDA electronic band structure and density of states for bcc Au at zero pressure. The energies are given relative to the Fermi level, the dotted line.

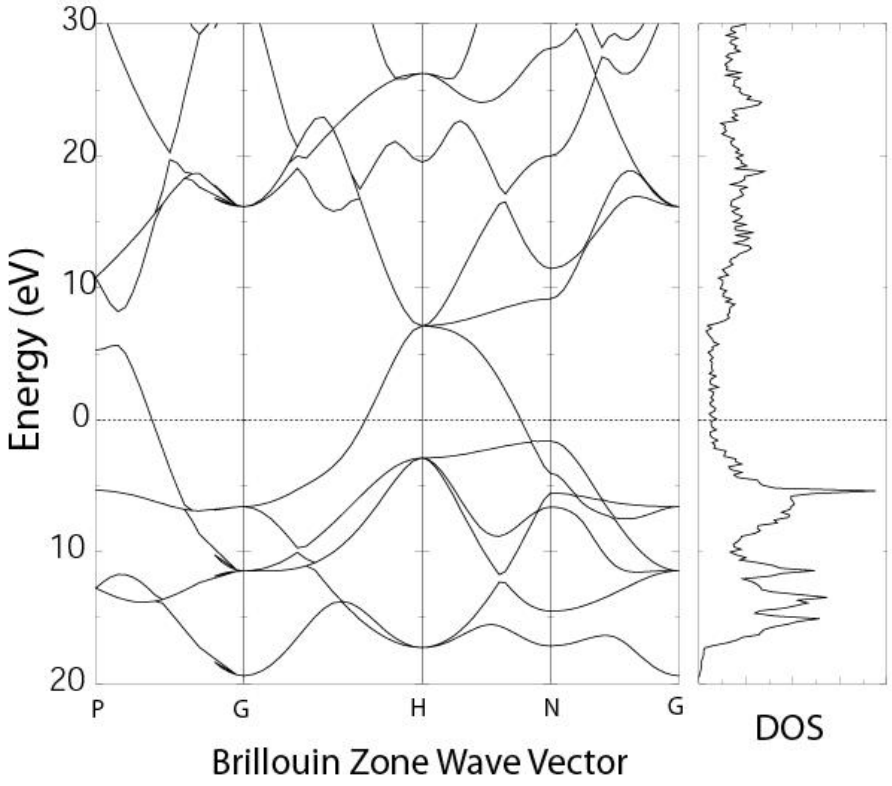

Figure 5.10: Scalar relativistic LDA electronic band structure and density of states for bcc Au at 600 GPa pressure. The energies are given relative to the Fermi level, the dotted line.

Chapter 6

PHONON DISPERSION RELATIONS

In order to calculate the phonon dispersion, probably harmonic approximation is the most convenient one. The starting point of the approximation is the potential energy (Eq. 6.1) [55] is expanded in forms of Taylor theorem and the terms higher than quadratic one are truncated.

$$U = \frac{1}{2} \sum_{\mathbf{R}\mathbf{R}'} \phi(\mathbf{R} - \mathbf{R}' + \mathbf{u}(\mathbf{R}) - \mathbf{u}(\mathbf{R}) - \mathbf{u}(\mathbf{R'})) \tag{6.1}$$

where $\mathbf{u}(\mathbf{R})$ is the displacement vector, U is the total potential energy and $\phi(\mathbf{r})$ is the energy contribution of two separated atoms by $\mathbf{r}$. After Taylor expansion Eq. 6.1 becomes

$$\begin{aligned} U = \frac{N}{2} \sum \phi(\mathbf{R}) + \frac{1}{2} \sum_{\mathbf{R}\mathbf{R}'} (\mathbf{u}(\mathbf{R}) - \mathbf{u}(\mathbf{R}')).\nabla\phi(\mathbf{R} - \mathbf{R}') \\ + \frac{1}{4} \sum_{\mathbf{R}\mathbf{R}'} \left[(\mathbf{u}(\mathbf{R}) - \mathbf{u}(\mathbf{R}')).\nabla\right]^2 \phi(\mathbf{R} - \mathbf{R}') \end{aligned} \tag{6.2}$$

Second term in Eq. 6.2 is vanish and first term equals to the equilibrium potential energy and a constant. Thus it can be omitted and only the quadratic term retains. The harmonic term can be written as a different form such that

$$U^{harm} = \frac{1}{2} \sum_{RR',\mu\nu} u_\mu(\mathbf{R}) D_{\mu\nu}(\mathbf{R} - \mathbf{R}') u_\nu(\mathbf{R}') \tag{6.3}$$

where

$$D_{\mu\nu}(\mathbf{R}-\mathbf{R}') = \delta_{\mathbf{R},\mathbf{R}'} \sum_{\mathbf{R}''} \phi_{\mu\nu}(\mathbf{R}-\mathbf{R}') - \phi_{\mu\nu}(\mathbf{R}-\mathbf{R}') \tag{6.4}$$

Eq. 6.3 can be written as the vector product of $\mathbf{u}(\mathbf{R})$ with the vector obtained by operating on the vector $\mathbf{u}(\mathbf{R}')$ with the matrix $\mathbf{D}(\mathbf{R}\text{-}\mathbf{R}')$ [55]. By considering the crystal symmetries we have the following $3N$ equations of motion as

$$M_\mu(\mathbf{R}) = -\frac{\partial U^{harm}}{\partial u_\mu(\mathbf{R})} = -\sum_{\mathbf{R}'_\nu} D_{\mu\nu}(\mathbf{R}-\mathbf{R}')u_\nu(\mathbf{R}') \tag{6.5}$$

or, in matrix notation

$$M(\mathbf{R}) = -\sum_{\mathbf{R}'} \mathbf{D}(\mathbf{R}-\mathbf{R}')\mathbf{u}(\mathbf{R}') \tag{6.6}$$

If we assume the solutions to the equations of motion in the form of plane waves, Eq. 6.5 becomes

$$M\omega^2\epsilon = \mathbf{D}(\mathbf{k})\epsilon \tag{6.7}$$

where ϵ is an eigenvector and $\mathbf{D}(\mathbf{k})$ is given

$$\mathbf{D}(\mathbf{k}) = \sum_{\mathbf{R}} \mathbf{D}(\mathbf{R}) exp(-i\mathbf{k}.\mathbf{R}) \tag{6.8}$$

$\mathbf{D}(\mathbf{k})$ is known as the dynamical matrix and three solutions of Eq. 6.7 gives the $3N$ normal modes.

The phonon frequencies of Au is obtained by calculating dynamical matrix at various volumes and symmetry directions. The supercell method and small-displacement method were used in the calculations. Fig. 6.1 shows the results and experimental data is also given in the figure. Our calculated phonon frequencies are in perfect agreement with experiment. As seen from the figure between $\Gamma - X$ and $\Gamma - L$ directions one transverse modes are degenerate and maximum frequency occurs at high symmetry L point. The Fig. 6.2 shows the phonon dispersion relations at 67 GPa. The form of the Fig. 6.2 is similar with Fig. 6.1. Thus, it seems that at all points frequencies shift by same amount. To understand the relation we calculated phonon frequencies at high symmetry points X, K and L and their pressure dependence is shown in Fig. 6.2. As seen from the figure after 100 GPa pressure the phonon frequencies increases linearly. Finally, the phonon density of states at various pressures (shown in Fig. 6.4) were calculated.

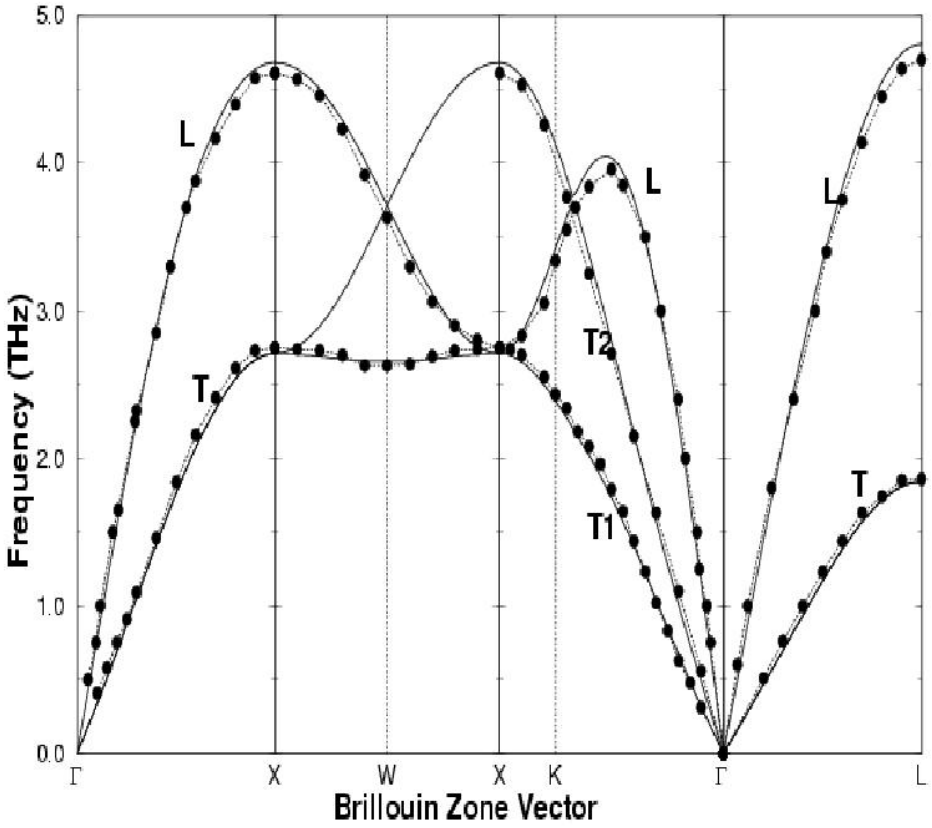

Figure 6.1: Phonon dispersion relation for fcc Au at zero pressure. The filled circles are the experimental data of Lynn *et al.* [29]. The high symmetry points and transverse and longitudinal branches are marked in the figure.

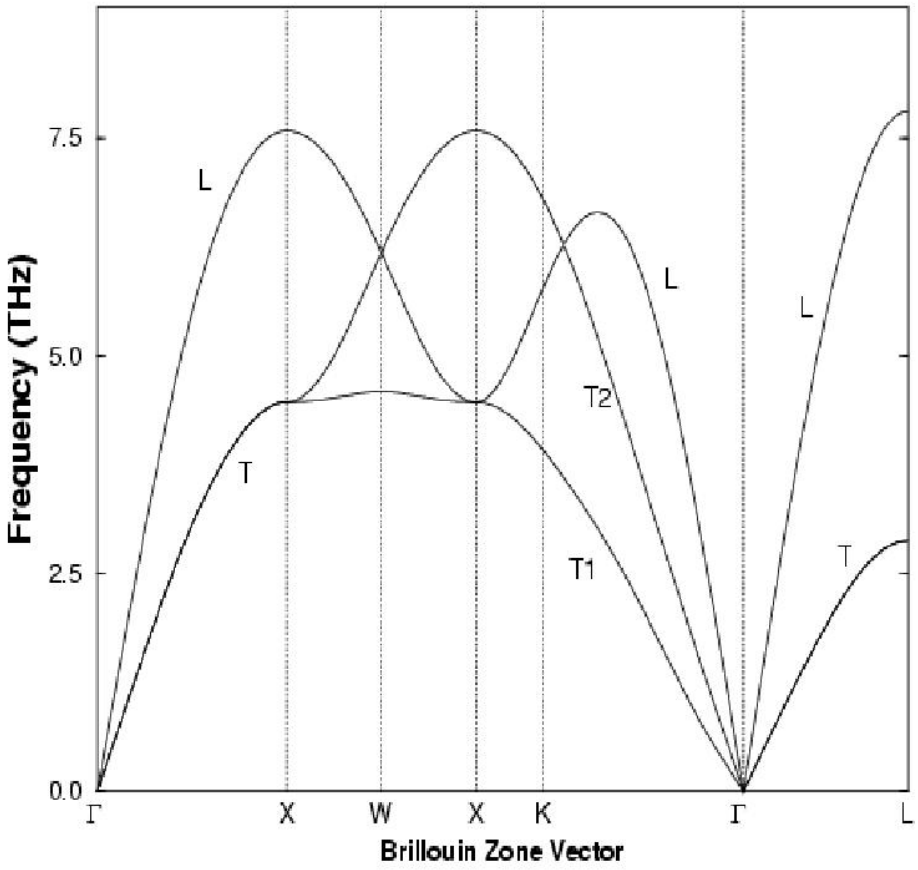

Figure 6.2: Phonon dispersion relation for fcc Au at 67 GPa pressure.

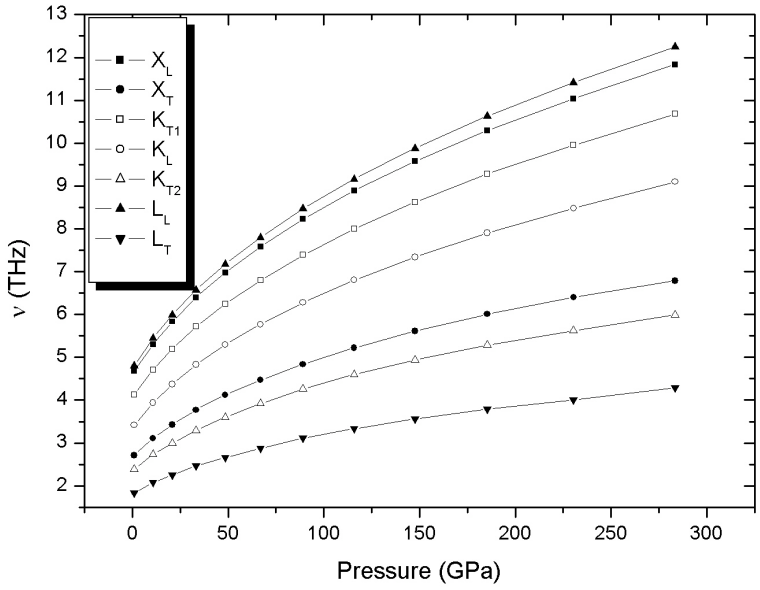

Figure 6.3: The variation of zone boundary phonons as a function of pressure.

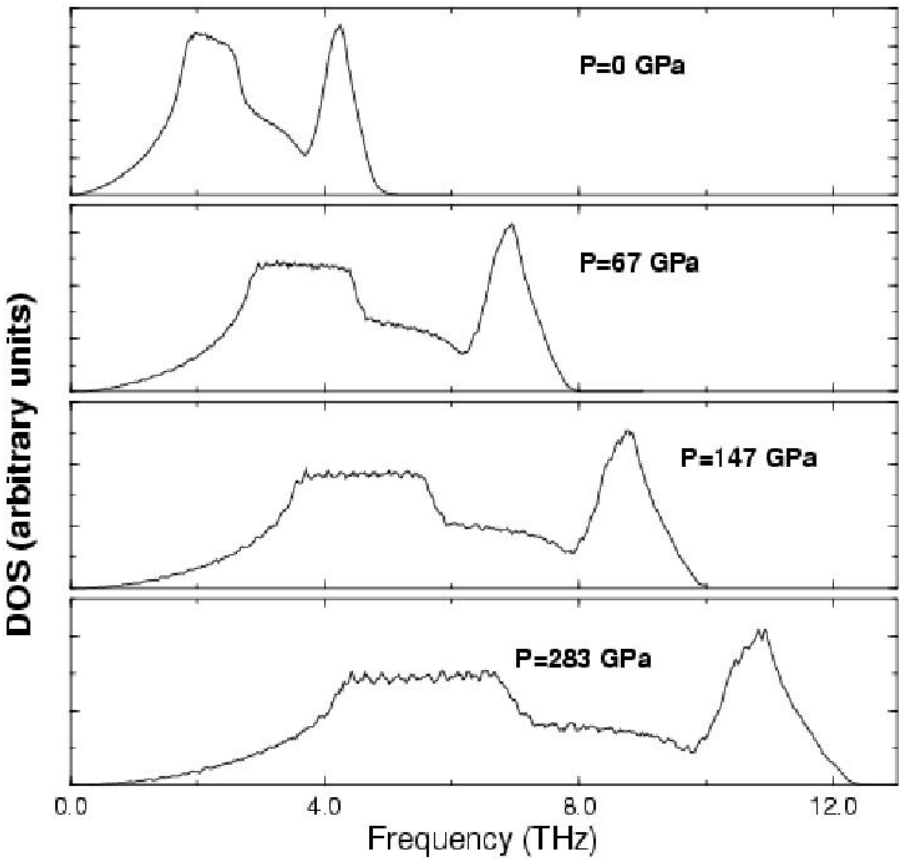

Figure 6.4: The phonon density of states at 0, 67, 147 and 283 GPa pressures.

Chapter 7

CONCLUSION

In this thesis the high pressure properties of Au is calculated from first principle calculations. The static equation of state is obtained up to 500 GPa pressure for two different approximations. Calculations on both GGA and LDA functionals show that LDA is better predicting the physical properties of metal Au. Moreover, it was seen that the Vinet type of EOS generates the equation of state of Au in the 0-500 GPa pressure regime. Furthermore, there is a phase transition from fcc to bcc phases at about 500 GPa. Below this pressure fcc phase stability is observed. The elastic properties of Au was calculated by applying three distinct deformations on fcc cell. The calculated elastic constants (i.e., three stiffness constants, tetragonal shear modulus and bulk modulus) are in agreement with previous theoretical and experimental studies. The pressure dependency of c_{44} is higher than c_S, thus the anisotropy pressure dependency is high. Moreover, the aggregate elastic properties and sound velocities were calculated via ab-initio calculation for Au. Band structure and density of states were calculated for fcc phase at 3 different pressures and bcc phase for 2 different pressure. At chapter 6, phonon dispersion relations for gold in the principal symmetry directions is calculated and observed that the calculated values are in perfect agreement with experiment. Furthermore, the pressure dependency of zone boundary phonon frequencies is obtained and have seen the linear relation after 100 GPa.

At this point our pressure dependent calculations are almost completed and

thermal effects should be included. The thermal equation of state can be calculated via Helmholtz free energy. These calculations will be performed in the near future.

Bibliography

[1] M. C. Payne, M. P. Teter, D. C. Allan, T. A. Arias, and J. D. Joannapoulos, Rev. Mod. Phys. **64**, 1045 (1992).

[2] D. R. Hartree, Proc. Cambridge. Philos. Soc. **24**, 89 (1928).

[3] J. C. Slater, Phys. Rev. **35**, 210 (1930).

[4] V. Fock, Z. Phys. **61**, 126 (1930).

[5] L. H. Thomas, Proc. Cambridge. Philos. Soc. **23**, 542 (1927).

[6] E. Fermi, Z. Phys. **48**, 73 (1928).

[7] See, e.g., N. H. March in *Theory of the inhomogeneous electron gas*, eds. S. Lundqvist and N. H. March (Plenum, NY, 1983).

[8] P. Hohenberg and W. Kohn, Phys. Rev. **136**, 864B (1964).

[9] W. Kohn and L. J. Sham, Phys. Rev. **140**, 1133A (1965).

[10] See, e.g., J. Kohanoff and N. Gidopoulos in *The Handbook of Molecular Physics and Quantum Chemistry. Ed S Wilson, Vol. 2, Molecular Electronic Structure, John Wiley and Sons*, (2002).

[11] D. C. Langreth and M. J. Mehl, Phys. Rev. Lett. **47**, 446 (1981); Phys. Rev. B **28**, 1809 (1983).

[12] J. P. Perdew and J. Wang, Phys. Rev. B **33**, 8822 (1986).

[13] J. P. Perdew and Y. Wang, Phys. Rev. B **45**, 13244 (1991).

[14] A. D. Becke, Phys. Rev. A **38**, 3098 (1988).

[15] J. Ihm, A. Zunger, and M. L. Cohen, J. Phys. C: Solid State Phys. **12**, 4409 (1979).

[16] E. Kaxiras, *Atomic and Electronic Structure of Solids* (Cambridge University Press, UK, 2003).

[17] D. J. Chadi and M. L. Cohen, Phys. Rev. B **8**, 5747 (1973).

[18] J. D. Joannopoulos and M. L. Cohen, J. Phys. C **6**, 1572 (1973).

[19] H. J. Monkhorst and J. D. Pack, Phys. Rev. B **13**, 5188 (1976).

[20] R. A. Evarestov and V. P. Smirnov, Phys. Status Solidi **119**, 9 (1983).

[21] J. C. Jamieson, J. N. Fritz, and M. H. Manghnani, in *High-Pressure Research in Geophysics*, edited by S. Akimoto and M. H. Manghnani (Center fo Academic Publishing, Tokyo, 1982), p.27.

[22] D. L. Heinz and R. Jeanloz, J. Appl. Phys. **55**, 885 (1984).

[23] F. Birch, J. Geophys. Res. **83**, 1257 (1978).

[24] F. Birch, Phys. Rev. B **71**, 809 (1947).

[25] F. Birch, Phys. Chem. Solids **38**, 175 (1977).

[26] B. Golding, S. C. Moss, and B. L. Averbach, Phys. Rev. B **158**, 637 (1967).

[27] Y. Hiki and A. V. Granato, Phys. Rev. B **144**, 411 (1966).

[28] W. B. Daniels and C. S. Smith, Phys. Rev. B**111**, 713 (1958).

[29] J. W. Lynn, H. G. Smith, and R. M. Nicklow, Phys. Rev. B **8**, 3493 (1973).

[30] T. S. Duffy, G Shen, D. L. Heinz, J. Shu, Y. Ma, H. K. Mao, R. J. Hemley, and A. K. Singh, Phys. Rev. B **60**, 15063 (1999).

[31] B. K. Godwal and R. Jeanloz, Phys. Rev. B **40**, 7501 (1989).

[32] P. Vinet, J. Ferrante, J. R. Smith, and J. H. Rose, J. Phys. C **19**, L467 (1986).

[33] P. Vinet, J. R. Smith, J. Ferrante, and J. H. Rose, Phys. Rev. B **35**, 1945 (1987).

[34] P. Vinet, J. Ferrante, J. H. Rose, and J. R. Smith, J. Geophys. Res. **92**, 9319 (1987).

[35] B. W. Dodson, Phys. Rev. B **35**, 2619 (1987).

[36] H. L. Skriver, *The LMTO Method* (Springer, Berlin, 1984).

[37] A. Khein, D. J. Singh, and C. J. Umrigar, Phys. Rev. B **51**, 4105 (1995).

[38] D. J. Singh, *Planewaves, Pseudopotential, and the LAPW Method* (Kluwer Academic, Boston, 1994).

[39] J. P. Perdew, J. A. Chevary, S. H. Vosko, K. A. Jackson, M. R. Pederson, D. J. Singh, and C. Fiolhais, Phys. Rev. B **46**, 6671 (1992).

[40] T. Tsuchiya and K. Kawamura, J. Chem. Phys. **116**, 2121 (2002).

[41] K. H. Weyrich, Phys. Rev. B **37**, 10269 (1988).

[42] J. C. Boettger, Phys. Rev. B **67**, 174107 (2003).

[43] A. B. Alchagirov, J. P. Perdew, J. C. Boettger, R. C. Albers, and C. Fiolhais, Phys. Rev. B **63**, 224115 (2001).

[44] R. Ahuja, S. Rekhi, and B. Johansson, Phys. Rev. B **63**, 212101 (2001).

[45] P. Söderlind, Phys. Rev. B **66**, 176201 (2002).

[46] C. W. Greeff and M. L. Graf, Phys. Rev. B **69**, 054107 (2004).

[47] G. Kresse and J. Hafner, Phys. Rev. B **47**, R558 (1993).

[48] D. Vanderbilt, Phys. Rev. B **41**, 7892 (1990).

[49] V. Voigt, *Lehrbuch der Kristallphysik* (Teubner, Berlin, reprinted 1928).

[50] A. Reuss, Z. Angew. Math. Mech. **9**, 55 (1929).

[51] G. Grimvall, *Thermophysical Properties of Materials* (Elsevier Science B. V., Amsterdam, 1999).

[52] R. Hill, J. Mech. Phys. Solids **11**, 357 (1963).

[53] P. Söderlind, O. Eriksson, J. M. Wills, and A. M. Boring, Phys. Rev. B **48**, 5844 (1993).

[54] E. B. Christoffel, Ann. Mat. Pura Appl. **8**, 193 (1877).

[55] N. W. Aschcroft and N. D. Mermin, *Solid State Physics* (Saunders College, Tokyo, 1981).